Induced quadrupolar singlet ground state of praseodymium in a modulated pyrochlore

J. van Duijn,[1,2,3,*] K. H. Kim,[4] N. Hur,[5] R. Ruiz-Bustos,[6] D. T. Adroja,[2] F. Bridges,[7] A. Daoud-Aladine,[2] F. Fernandez-Alonso,[2,8] J. J. Wen,[9] V. Kearney,[7] Q. Z. Huang,[10] S.-W. Cheong,[5] T. G. Perring,[2] and C. Broholm[9,10]

[1]*Department of Physics and Astronomy, John Hopkins University, Baltimore, Maryland 21218, USA*

[2]*ISIS Facility, Rutherford Appleton Laboratory, Chilton, Didcot, OX11 0QX, United Kingdom*

[3]*Instituto de Investigación en Energías Renovables, Departamento de Física Aplicada, Universidad de Castilla-La Mancha, Albacete, 02006, Spain*

[4]*CeNSCMR, Department of Physics and Astronomy, Seoul National University, Seoul 151-747, South Korea*

[5]*Rutgers Center for Emergent Materials and Department of Physics and Astronomy, Rutgers University, Piscataway, New Jersey 08854, USA*

[6]*Departamento de Mecánica, Universidad de Córdoba, Córdoba, 14071, Spain*

[7]*Department of Physics, University of California, Santa Cruz, California 95064, USA*

[8]*Department of Physics and Astronomy, University College London, Gower Street, London, WC1E 6BT, United Kingdom*

[9]*Institute for Quantum Matter and Department of Physics and Astronomy, Johns Hopkins University, Baltimore, Maryland 21218, USA*

[10]*NIST Center for Neutron Research, National Institute of Standards and Technology, Gaithersburg, Maryland 20899, USA*

(Received 2 July 2014; revised manuscript received 25 July 2017; published 11 September 2017)

The complex structure and magnetism of $Pr_{2-x}Bi_xRu_2O_7$ was investigated by neutron scattering and extended x-ray absorption fine structure. Pr has an approximate doublet ground state and the first excited state is a singlet. While the *B*-site (Ru) is well ordered throughout, this is not the case for the *A*-site (Pr/Bi). A broadened distribution for the Pr-O2 bond length at low temperature indicates the Pr environment varies from site to site even for $x = 0$. The environment about the Bi site is highly disordered ostensibly due to the 6*s* lone pairs on Bi^{3+}. Correspondingly, we find that the non-Kramers doublet ground-state degeneracy, otherwise anticipated for Pr in the pyrochlore structure, is lifted so as to produce a quadrupolar singlet ground state with a spatially varying energy gap. For $x = 0$, below T_N, the Ru sublattice orders antiferromagnetically, with propagation vector $\mathbf{k} = (0,0,0)$ as for $Y_2Ru_2O_7$. No ordering associated with the Pr sublattice is observed down to 100 mK. The low-energy magnetic response of $Pr_{2-x}Bi_xRu_2O_7$ features a broad spectrum of magnetic excitations associated with inhomogeneous splitting of the Pr quasidoublet ground state. For $x = 0$ ($x = 0.97$), the spectrum is temperature dependent (independent). It appears disorder associated with Bi alloying enhances the inhomogeneous Pr crystal-field level splitting so that intersite interactions become irrelevant for $x = 0.97$. The structural complexity for the *A*-site may be reflected in the hysteretic uniform magnetization of *B*-site ruthenium in the Néel phase.

DOI: 10.1103/PhysRevB.96.094409

I. INTRODUCTION

In pyrochlore materials, with the general formula $A_2B_2O_7$, the *A*- and *B*-site ions form an interpenetrating network of corner-sharing tetrahedra [1]. When populated by magnetic ions with nearest-neighbor antiferromagnetic (AFM) interactions, these materials display anomalous frustrated magnetism [2]. The resulting low-temperature phases include spin glasses, spin liquids, and magnetoelastically induced Néel order [3–7]. While the majority of pyrochlore magnets are insulators, an interplay between magnetism and strong electron correlations can occur when the *B*-site is occupied by a magnetic 4*d* or 5*d* ion.

Focusing only on materials in which the *B*-site is wholly occupied by a magnetic 4*d* or 5*d* ion, stable pyrochlore structures have been reported for *B* = Nb, Mo, Ru, Re, Os, Ir, and Pt [8]. In the Nb pyrochlores (which are all insulating), the Nb^{4+} ions are expected to have spins $S = \frac{1}{2}$, however, magnetization and specific-heat measurements show the Nb sublattice to be nonmagnetic [9,10]. While density functional theory (DFT) indicates a metallic state, there is a metal insulator (MI) transition that results in local singlet formation [11]. MI transitions have been observed in the Mo, Ru, and Ir family of pyrochlores [12–17]. Aside from MI transitions, heavy-fermion behavior and anomalous Hall effect have also been observed in the Mo and Ir pyrochlores, e.g., $Nd_2Mo_2O_7$ and $Pr_2Ir_2O_7$ [18–20]. A robust spin-glass state with the requisite scaling and aging is observed in spin-1 $Y_2Mo_2O_7$ [21,22]. Quenched local disorder that modulates superexchange interactions through orbital disorder is now thought to underlay this state [23]. Superconducting transitions have been observed for $Cd_2Re_2O_7$ and the osmium family of beta-pyrochlores (AOs_2O_6) [24–28].

The ruthenium pyrochlores display a variety of ground states near the above-mentioned MI transition [15,16,29–36]. In this family of materials, the MI transition is correlation induced. Band structure calculations show that their electronic bandwidths are strongly influenced by the Ru-O-Ru bond angle, which in turn is controlled by the ionic radius of the A^{3+} ion [14]. As a result, $A_2Ru_2O_7$ (A = Y, rare earths) are insulating with long-range magnetic order, while $Bi_2Ru_2O_7$ is a Pauli paramagnet. $Tl_2Ru_2O_7$ is a metal at room temperature and a spin-singlet insulator below 120 K. Bulk measurements show antiferromagnetic ordering of the Ru sublattice for the insulating compounds with a critical temperature T_N, that decreases monotonically from 160 K for Pr to 81 K for Yb, consistent with the lanthanide contraction [31]. The

*Present address: Departamento de Mecánica, Universidad de Córdoba, Córdoba, 14071, Spain; Corresponding author: me2vavaj@uco.es

temperature and energy scale of the magnetic interactions on the rare-earth sublattice are an order of magnitude lower than for the transition-metal B-site [15,16,32–34].

In this paper, we examine the structure and magnetism of $Pr_{2-x}Bi_xRu_2O_7$ solid solutions [37]. Bulk measurements show substituting Bi^{3+} for Pr^{3+} drives the system from an antiferromagnetic insulator ($x = 0$) to a Pauli paramagnetic metal ($x = 2$). While this transition has been observed in other Ru pyrochlores, in $Pr_{2-x}Bi_xRu_2O_7$ the low-T specific heat is greatly enhanced, reminiscent of non-Fermi-liquid and heavy-fermion systems. Aside from influencing the Ru-O-Ru bond angle and hence the electronic bandwidths, replacing Pr^{3+} by Bi^{3+} also introduces structural disorder due to the 6s lone pair electrons of the Bi^{3+} cations. Recent work on $Bi_2B_2O_7$ (B = Ti, Zn, Nb, Ru, Sn, and Hf) shows that in the pyrochlore structure, the Bi^{3+} lone pairs induce local site distortions, resulting in cation off centering via incoherent disorder rather than ordered noncubic ground states [38–41]. Recent high-resolution neutron powder diffraction experiments on $Bi_2Ti_2O_7$ and $Bi_2Ru_2O_7$ show that, in $Bi_2Ti_2O_7$ (which is insulating) this disorder has the effect of stabilizing the Bi^{3+} valence while simultaneously satisfying the steric constraint imposed by the lone pair electrons [42,43]. In metallic $Bi_2Ru_2O_7$, on the other hand, off centering is not required to satisfy the Bi^{3+} valence but seems to be driven solely by the presence of the lone pair. As a result, these nonmagnetic lone-pair-containing pyrochlore compounds can be regarded as systems with a high degree of static local disorder [42].

We find for $Pr_{2-x}Bi_xRu_2O_7$ that Pr, assuming the ideal pyrochlore structure, has a quasidoublet ground state and a singlet excited state. In previous inelastic neutron scattering experiments, we showed the enhanced low-T specific heat and heavy-fermion-like properties are a consequence of a static inhomogeneous splitting of the non-Kramers Pr^{3+} ground-state doublet. Here, we show that even without Bi substitution in $Pr_2Ru_2O_7$, the ground-state degeneracy anticipated for non-Kramers praseodymium in the pyrochlore lattice A-site is lifted. This is evidence of a local structural distortion that breaks the threefold rotation axis. Through extended x-ray absorption fine structure (EXAFS) measurements, we provide direct structural evidence for a distribution of coordinating environments for praseodymium in $Pr_2Ru_2O_7$. While the B-site (Ru) environment remains well ordered throughout the series, the A-site becomes progressively disordered with increasing x, primarily near bismuth. For the end compound $Bi_2Ru_2O_7$, previous diffraction studies have shown the Bi displacement to be perpendicular to the Bi-O2 axis [38]. We observe a similar off-center displacement of Bi, both in this material and in the substituted material $Pr_{1.03}Bi_{0.97}Ru_2O_7$.

For $x = 0$, below T_N, the Ru sublattice orders in a similar arrangement as for $Y_2Ru_2O_7$, so this order does not appear to be influenced by the Pr rare-earth anisotropy [31]. For the Pr sublattice, however, no order is detected by diffraction down to 1.5 K for any x. The specific heat has a Schottky-like anomaly centered at 3 K but no further anomalies associated with magnetic ordering at least down to 0.1 K. Probed by inelastic neutron scattering, the low-energy magnetic excitation spectrum of $Pr_{2-x}Bi_xRu_2O_7$ shows the corresponding mode of excitation. In the temperature dependence of the excitation spectrum, we provide evidence for collective effects from Pr-Pr interactions for $Pr_2Ru_2O_7$, these, however, vanish for $x = 0.97$ where the temperature dependence of the inelastic scattering can be described by inhomogeneous single-ion physics.

II. EXPERIMENTAL TECHNIQUES

Powdered samples of $Pr_{2-x}Bi_xO_7$ ($x = 0$, 0.97, and 2) were synthesized using the solid-state reaction method. For the Ru-containing samples, mixtures of Pr_2O_3, Bi_2O_3, and RuO_2 in proper molar ratios were prereacted at 850 °C for 15 h in air. The samples were subsequently ground, pressed into pellets and sintered at 1000 °C–1200 °C in air with intermediate grindings. All samples were characterized by powder x-ray diffraction. These measurements showed the samples all adopt the cubic pyrochlore structure and are single phase, except for the $x = 0$ sample, which contained 3.38(5)% by mass of unreacted RuO_2. Detailed bulk measurements on these samples have been reported elsewhere [37,44].

For the heat capacity measurement, $Pr_2Ru_2O_7$ powder was thoroughly mixed with silver powder, 50% by weight, and cold pressed into a solid pellet to achieve adequate thermal conductivity. Data were collected down to 90 mK with the adiabatic relaxation method using a commercial Physical Property Measurement System (PPMS) Dilution Refrigerator. The specific-heat capacity of $Pr_2Ru_2O_7$ was obtained by subtracting the measured specific-heat capacity of silver from the measured total heat capacity [45].

EXAFS studies at 4 K were carried out at the Stanford Synchrotron Radiation Lightsource (SSRL) at all the metal edges in $Pr_{2-x}Bi_xRu_2O_7$ for $x = 0$, 0.97, and 2, using an Oxford He cryostat. Transmission mode EXAFS data were collected for the Pr L_{III} edge (5964 eV), the Bi L_{III} edge (13 419 eV), and the Ru K edge (22 117 eV). We used a Si (220) double monochromator for the Ru edge and Si (111) crystals for the Bi and Pr L_{III} edges. The slit height was 0.5 mm, giving energy resolutions of 1 eV for the Pr L_{III} edge, and ~2.7 eV for the Bi L_{III} and the Ru K edge. The monochromator was detuned 50% for the Pr and Bi L_{III} edges and 30% for the Ru K edge to minimize harmonics. EXAFS samples were prepared by first brushing fine powder ($\leqslant 5\,\mu$m) onto scotch tape; two pieces of tape were then pressed together (double layer) to encapsulate the powder. For the Ru edge we used 7, 9, and 15 double layers for $x = 2$, 0.97, and 0, respectively. Three double layers were used for the Bi L_{III} edges, and two double layers for the Pr L_{III} edges.

Standard procedures were used to reduce the EXAFS data [46]. First, a pre-edge subtraction was done to remove absorption from other atoms; this yields the absorption edge of interest μ_{edge}. Then, a spline was fit through the data above the edge to obtain an estimate of the absorption, $\mu_0(E)$, with no photoelectron backscattering. Next, the EXAFS oscillations $\chi(E)$ were obtained from $\mu_{edge} = \mu_0(E)[1+\chi(E)]$, and $\chi(E)$ converted to $\chi(k)$ using $\hbar^2\, k^2/2m = E - E_0$, where E_0 is the absorption edge energy. Finally, $k\chi(k)$ was Fourier transformed (FT) into r space, where peaks correspond to various neighboring shells about the absorbing atom.

Powder neutron diffraction data were collected on the $x = 0$ sample at the National Institute of Standards and Technology in Gaithersburg, Maryland (BT1) and at the ISIS Facility, Rutherford Appleton Laboratory, UK (HRPD). For the BT1

experiment, a 10-g sample was sealed in a vanadium container with length 50 mm and diameter 10.8 mm and the temperature was controlled in a He flow cryostat. A Ge (311) monochromator with a 90° take-off angle ($\lambda = 2.079$ Å) and in-pile collimation of 15 min of arc were used. Data sets were collected for temperatures between 1.5 and 180 K and scattering angle 2θ from 3°–168° with a step size of 0.05°. For the HRPD experiment, a 10-g sample was placed in a vanadium container 15 mm × 20 mm × 10 mm (h × w × d) within a He flow cryostat. Data sets were collected for temperatures between 2 and 300 K, using 10 to 110 ms chopper settings to sample a d-space range from 0.3 to 2.2 Å in the backscattering bank. Rietveld analysis of the neutron powder diffraction patterns was performed using the FULLPROFsuite software package [47].

Inelastic neutron scattering experiments were carried out at the ISIS Facility, Rutherford Appleton Laboratory, UK. High-energy data were collected on all samples using the time-of-flight (TOF) spectrometer HET. Additional low-energy data were collected on the $x = 0$ sample using the IRIS spectrometer [48,49]. For the HET experiment, the samples were loaded in an Al sachet and the total mass of sample in the beam was 19.2 g for $x = 0$, 24.9 g for $x = 0.97$, and 22.55 g for $x = 2$. The samples were top loaded into a closed-cycle He refrigerator. Incident energies of $E_i = 35$ and 160 meV were employed with a full width at half maximum (FWHM) energy resolution at the elastic line of 1.4 and 7 meV, respectively. Data were collected at 5 and 200 K. More details on normalization and the correction for the phonon contribution to the scattering data will be provided below. Crystal-field (CF) analysis of the data was performed using the FOCUS program [50].

The IRIS experiment was carried out on 15 g of $Pr_2Ru_2O_7$. The sample was held in a sealed 2-mm double-walled Al can with diameter 23 mm and height 53 mm and loaded into a He cryostat. Bandwidth disk choppers selected an incident spectrum from 1.35 to 4.6 meV pulsed at 25 Hz and a backscattering pyrolytic graphite analyzer bank with a 25-K Be filter selected the final energy, $E_f = 1.847$ meV. The FWHM elastic energy resolution was 17.5 μeV. Data were collected over a temperature range from 1.5 to 200 K.

Neutron scattering theory indicates that in a cubic system containing magnetic rare-earth ions, the single-ion susceptibility is related to the eigenfunctions and energies of the CF Hamiltonian via the following equation [51–53]:

$$\chi_0^{\alpha\beta}(\omega) = (g\mu_B)^2 \lim_{\epsilon\to 0^+}\left[\sum_{\substack{p,q\\ E_p\neq E_q}} \frac{\langle p|J_\alpha|q\rangle\langle q|J_\beta|p\rangle}{E_p - E_q - \omega - i\epsilon}(n_q - n_p) + \frac{1}{k_B T} \times \frac{\epsilon}{\epsilon - i\omega}\left(\sum_{\substack{p,q\\ E_p=E_q}} \langle p|J_\alpha|q\rangle\langle q|J_\beta|p\rangle n_p - \langle J_\alpha\rangle\langle J_\beta\rangle\right)\right]. \quad (1)$$

Here, J_α indicates a Cartesian component ($\alpha = x,y,z$) of the angular momentum operator, $|p\rangle$ and E_p are the eigenfunctions and energies of the crystal-field Hamiltonian $\mathcal{H}_{\rm CF}$. Finally, n_p is the thermal population factor, which is defined as $n_p = \mathcal{Z}^{-1}\exp(-\beta E_p)$. Here, $\mathcal{Z}$ is called the partition function and is written as $\mathcal{Z} = \sum_q \exp(-\beta E_q)$. The intersite interactions have been treated using the random phase approximation. For Pr^{3+} ions in the ideal pyrochlore structure, the ninefold-degenerate free-ion ground-state J multiplet $^4H_3$ should split into 3 doublets and 3 singlets under the effect of the D_{3d} symmetric $\mathcal{H}_{\rm CF}$. Choosing [111] as the quantization axis, the single-ion crystal-field Hamiltonian takes the form

$$\mathcal{H}_{\rm CF} = B_2^0 O_4^0 + B_4^0 O_4^0 + B_4^3 O_4^3 + B_6^0 O_6^0 + B_6^3 O_6^3 + B_6^6 O_6^6, \quad (2)$$

where B_n^m are the CF parameters and O_n^m are Stevens operator equivalents of the CF tensor operators as discussed by Hutchings [54]. Here, the CF interaction in the LS coupling scheme is treated as a perturbation within the ground-state J multiplet only.

The following corrections were applied to the neutron counts in the time histograms collected on both HET and IRIS. First, a time-independent background measured for $\hbar\omega \approx -E_f$ was subtracted. Then, the data were scaled to the relevant count rate in a presample monitor and converted into $\hbar\omega$ histograms. This procedure gives $\hbar\omega$-dependent data $I(Q,\hbar\omega)$, which are related to the scattering cross section through convolution with a resolution function, as follows:

$$I(Q,\hbar\omega) = \mathcal{C}N \int dQ'\hbar\, d\omega' R_{Q\omega}(Q - Q',\omega - \omega') \times \frac{k_i}{k_f}\frac{d^2\sigma}{d\Omega\, dE'}(Q',\omega'), \quad (3)$$

where N is the number of formula units in the sample, and $\mathcal{C}$ is the spectrometer constant. Here, the instrumental resolution function $R_{Q\omega}$ is unity normalized:

$$1 \equiv \int R_{Q\omega}(Q - Q',\omega - \omega') dQ' d\omega'. \quad (4)$$

We define the normalized intensity $\tilde{I}(Q,\hbar\omega)$ as follows:

$$\tilde{I}(Q,\hbar\omega) \equiv \frac{I(Q,\hbar\omega)}{\mathcal{C}N}. \quad (5)$$

Thus, $\tilde{I}(Q,\hbar\omega)$ is the resolution smeared partial differential scattering cross section per formula unit which we express in absolute units of mbarn sr^{-1} meV^{-1} $f.u.^{-1}$.

For the HET experiment, $\mathcal{C}N$ was determined by measuring the incoherent scattering from a standard flat vanadium slab sample for each of the chosen incident energies. For the IRIS experiment, $\mathcal{C}N$ was determined from Bragg scattering through a method that has been described elsewhere [55]. These procedures yield absolute measurements of $\tilde{I}(Q,\hbar\omega)$ to an overall scale accuracy of 20%.

III. RESULTS

A. EXAFS measurements

The detailed local structure about the A-site (Pr or Bi) is shown in Fig. 1. There are three Pr atoms above and below the central atom forming two tetrahedra. The O2 atom (light blue) is in the center of each tetrahedra while the six O1 atoms

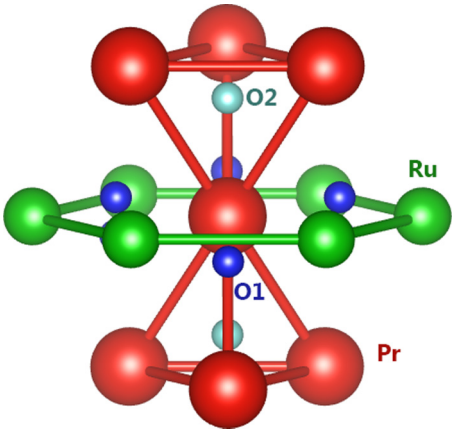

FIG. 1. Local structure about the A-site (Pr or Bi, large red atom) with no distortions present. The Pr atoms form two tetrahedra, corner linked at the central atom. The O2 atoms (small light blue) are at the center of each Pr tetrahedron. The nearest Ru atoms (green) form a hexagon in a plane perpendicular to the Pr-O2 (vertical) axis, while the six nearest O1 atoms (small blue, some hidden) are in a corrugated ring roughly perpendicular to the Pr-O2 axis. The B-site environment is very similar with Ru interchanged with Pr, but there are no oxygen atoms inside the Ru tetrahedra.

(dark blue) are roughly in a plane perpendicular to the Pr-O2 vertical axis. These O1 atoms are slightly displaced above and below the normal plane to the Pr-O2 axis that contains the Pr atom. Finally, the nearest B-site (Ru) atoms form a hexagon of (green) atoms in a plane perpendicular to this same plane. The corresponding B-site (Ru) environment is nearly identical, but there are no O atoms inside the Ru tetrahedra.

To investigate possible distortions in this local structure, we carried out EXAFS measurements at each metal edge and reduced the data as described above. In Figs. 2(a) and 2(b), we plot the r-space data [FT$k\chi(k)$], at 4 K, solid squares) for the A-site atoms (Pr and Bi) in the end compounds $x = 0$ and 2. The first peak in each scan is the metal-O peak, near 2.0–2.5 Å; a sum of Pr-O2 (2.243 Å) and Pr-O1 (2.546 Å) for the Pr L_{III} edge, and Bi-O2 (2.228 Å) and Bi-O1 (2.538 Å) peaks for the Bi L_{III} edge. The next peak (near 3.3 Å) is a combination of metal-metal peaks, i.e., for $x = 0$ at the Pr edge it would be a sum of Pr-Ru and Pr-Pr peaks. Corresponding peaks occur for the Pr and Bi edges in the mixed sample $Pr_{1.03}Bi_{0.97}Ru_2O_7$ [Figs. 2(e) and 2(f)].

Note that the peaks in the EXAFS spectra are shifted to lower r compared to the actual distances, by a well-known phase factor [56]. For example, the two Pr-O peaks in the simulated EXAFS spectra of Fig. 2(a) are located at ∼1.8 and 2.1 Å if plotted separately, a shift of roughly −0.45 Å relative to the actual distances in the model. For these peaks, the r-space phase (real part of the transform) of the peak for the shortest Pr-O2 distance (two O2 neighbors located inside the Bi/Pr tetrahedra) is nearly out of phase with that for the longer distance Pr-O1 peak (six neighbors), leading to an interference dip in the spectra at 1.8 Å.

To identify where significant differences exist between EXAFS and diffraction results, we used the ordered pyrochlore

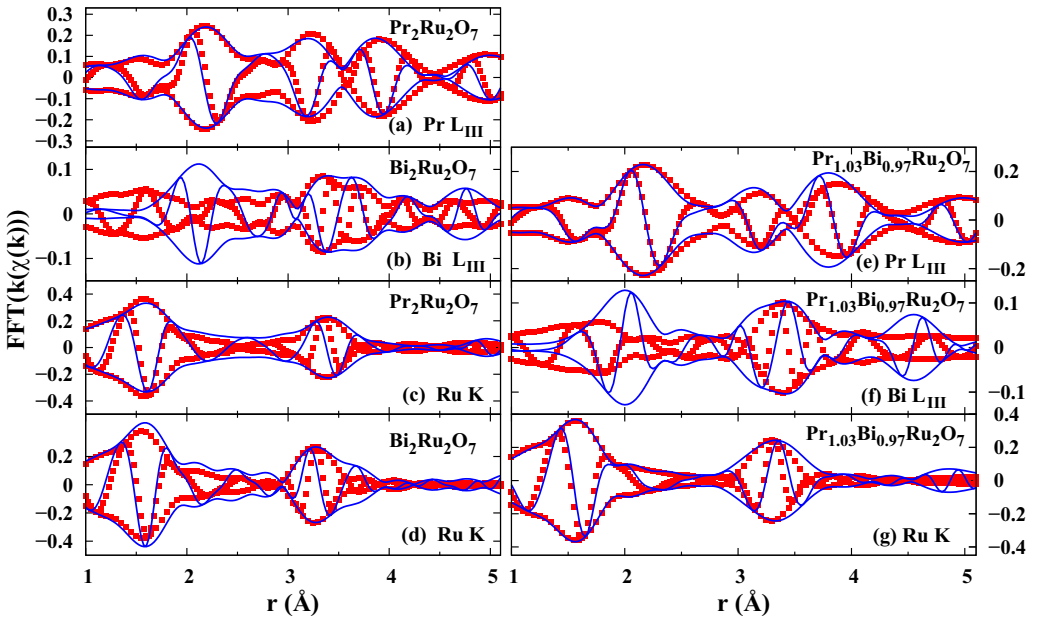

FIG. 2. EXAFS r-space data at $T = 4$ K. In this and subsequent r-space plots, the fast oscillation is the real part R of the FT while the envelope function is $\pm\sqrt{R^2 + I^2}$ where I is the imaginary part of the FT. (a) The Pr L_{III}, (b) the Bi L_{III}, and (c), (d) for the Ru K edges for $x = 0$ and 2, respectively. The corresponding data for $x = 0.97$ are shown in (e) Pr L_{III}, (f) Bi L_{III}, and (g) Ru K edge. In each plot, the data are shown as solid squares, while the solid lines are simulations (not a fit) based on the ordered pyrochlore structure from diffraction; they are calculated using the program FEFF8.2 plus a global broadening parameter σ to adjust the amplitude near 3 Å. For pure samples we used $\sigma =$ 0.07 Å for Pr, 0.08 Å for Bi, and for Ru, 0.0725 Å for $x = 0$ and 0.05 Å for $x = 2$. In the mixed sample, $\sigma = 0.06$ Å for Pr, 0.065 Å for Bi, and 0.05 Å for Ru. The largest deviations are for the Bi L_{III} edge at the first-neighbor O peak near 2 Å (a sum of Bi-O1 and Bi-O2 contributions). The FT ranges are Pr L_{III}, 3.5–10 $\mathrm{Å}^{-1}$; Ru K, 4.5–14 $\mathrm{Å}^{-1}$; and Bi L_{III}, 4–14 $\mathrm{Å}^{-1}$; with a Gaussian rounding of the transform window by 0.3 $\mathrm{Å}^{-1}$.

structure (from diffraction) and the program FEFF8.2 to calculate an r-space EXAFS function for each sample/edge [38,57]. We emphasize that *no fitting* is involved; however, we did adjust the overall amplitude so that the calculated peaks in the 3–4 Å range agreed with the data. This can be accomplished using either a multiplicative constant or a global broadening; we used the latter (see figure captions for details). The diffraction-based simulations are shown on each plot as solid blue lines.

These simulations show the environment about Pr to be relatively well ordered for both the pure and mixed samples; i.e., the shapes, positions, and amplitudes of the simulated peaks are close to that of the data (some disorder for Pr-O2 and Pr-Pr is discussed later). In contrast, there is considerable disorder about the Bi site in both $Bi_2Ru_2O_7$ and the mixed sample; in particular, the Bi-O peak which should occur near 2.1 Å in the data is strongly suppressed; it is much smaller and more spread out than in the simulation for the ordered pyrochlore structure.

The Ru K-edge data (solid squares) for the two pure samples are shown in Fig. 2; (c) $x = 0$, (d) $x = 2$, while the corresponding results for the mixed sample are plotted in Fig. 2(g). For Ru, there are six O1 neighbors which form a single Ru-O1 peak near 1.6 Å (actual distance ~2.02 Å). The second peak is a sum of Ru-Ru and either Ru-Pr ($Pr_2Ru_2O_7$) or Ru-Bi ($Bi_2Ru_2O_7$) for the pure samples. For the mixed sample, this peak is a sum of Ru-Ru, Ru-Pr, and Ru-Bi, which cannot be resolved. Consequently, for the Ru edge we focus on the Ru-O1 pair; for all samples, the Ru-O1 peak is large and the shape and amplitude agree well with the simulation. This indicates little disorder for the Ru-O1 pair in any sample, which in turn suggests that the O1 atoms are not significantly displaced within a plane roughly perpendicular to the Bi-O2 axis (see Fig. 1). Thus, for the Bi-O1 peak to be disordered (within this plane), Bi must be displaced from the usual A-site position, in a direction perpendicular to the Bi-O2 axis. This likely also leads to a small distortion of the Bi-O2 bonds.

We find similar results at higher temperatures; the Ru-O and most Pr-O peaks are generally well ordered while the Bi-O peak is strongly suppressed, indicating significant disorder. We also find that the Pr-Ru, Ru-Pr, and Ru-Ru second-neighbor peaks are reasonably ordered, but when Bi is present, peaks that include Bi second neighbors (e.g., Pr-Bi or Ru-Bi) are significantly broadened, leading to a low EXAFS amplitude.

B. Crystal-field measurements

To determine the crystal-field level scheme and the relevant low-energy spin degrees of freedom, we carried out high-energy inelastic neutron scattering measurements on HET. The nonmagnetic phonon contribution at low angles ($2\theta \approx 19^\circ$) was estimated (and subsequently subtracted) from the measured scattering at high scattering angles, where the magnetic response is negligible ($2\theta \approx 135^\circ$). This was done using an energy-dependent scaling factor determined from direct measurements on the Pauli paramagnetic compound $x = 2$. This procedure is based on two assumptions. First, the magnetic scattering intensity, which is proportional to the square of the Pr^{3+} magnetic form factor, is negligible in the high-angle scattering data. Second, the energy-dependent ratio between phonon scattering at low and high scattering angles is the same for all three compounds.

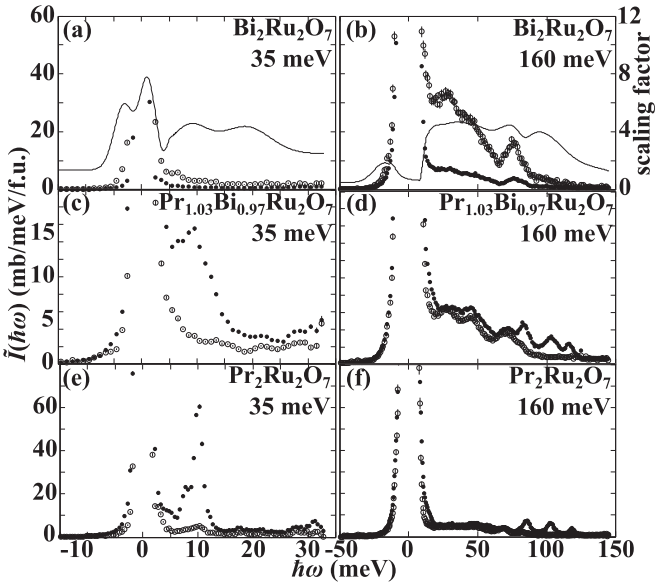

FIG. 3. Inelastic neutron scattering from $Pr_{2-x}Bi_xRu_2O_7$ for $x = 2$ (a), (b), $x = 0.97$ (c), (d), and $x = 0$ (e), (f) taken at 5 K and $E_i = 35$ and 160 meV. The spectra taken at low scattering angles ($2\theta = 19^\circ$, $Q_{el} = 1.36$ and 2.91 Å^{-1}, respectively) are shown as • whereas those taken at high scattering angles ($2\theta = 135^\circ$, $Q_{el} = 7.62$ and 16.30 Å^{-1}, respectively) are shown as ○. The solid line in (a) and (b) shows the energy-dependent scaling factor as determined from fits to the $x = 2$ data. For $x = 0.97$ and 0, the high-angle data have been scaled using the energy-dependent scaling factor to show the estimate of the nonmagnetic phonon contribution to the low-angle data. The plotted error bars indicate the interval of one standard deviation above and one standard deviation below the average corresponding to a confidence level of 68%. This convention is followed throughout the paper.

Figure 3 shows the total spectra for $Pr_{2-x}Bi_xRu_2O_7$ with $x = 2, 0.97$, and 0 measured at 5 K with incident energies $E_i = 35$ and 160 meV for low ($2\theta \approx 19^\circ$) and high ($2\theta \approx 135^\circ$) scattering angles. For $x = 0.97$ and 0, the high-angle spectra have been scaled down by the energy-dependent scaling factor determined from the $x = 2$ data [solid lines in Figs. 3(a) and 3(b)]. At low scattering angles, corresponding to $Q_{el} = 1.36$ Å^{-1} and 2.91 Å^{-1}, respectively, the spectra from $x = 0.97$ and 0 contain both magnetic and phonon contributions. In the high scattering angles spectra, corresponding to $Q_{el} = 7.62$ and 16.30 Å^{-1}, respectively, however, the magnetic contributions are small due to the very small form factor for Pr $4f$ electrons at such large-Q values. As shown in Figs. 3(a) and 3(b), the inelastic response of $x = 2$ shows three clear peaks due to one-phonon scattering at 30, 45, and 75 meV. These features are reproduced in the scaled high-angle scattering data of $x = 0.97$ and 0, indicating that the phonon scattering is indeed similar for all three compounds. This justifies use of the scaling method to estimate the phonon contribution to the low scattering angle spectra for the $x = 0$ and 0.97 samples. Figures 4 and 5 show magnetic scattering from $Pr_{2-x}Bi_xRu_2O_7$ after subtracting the phonon and elastic scattering, at 5 and

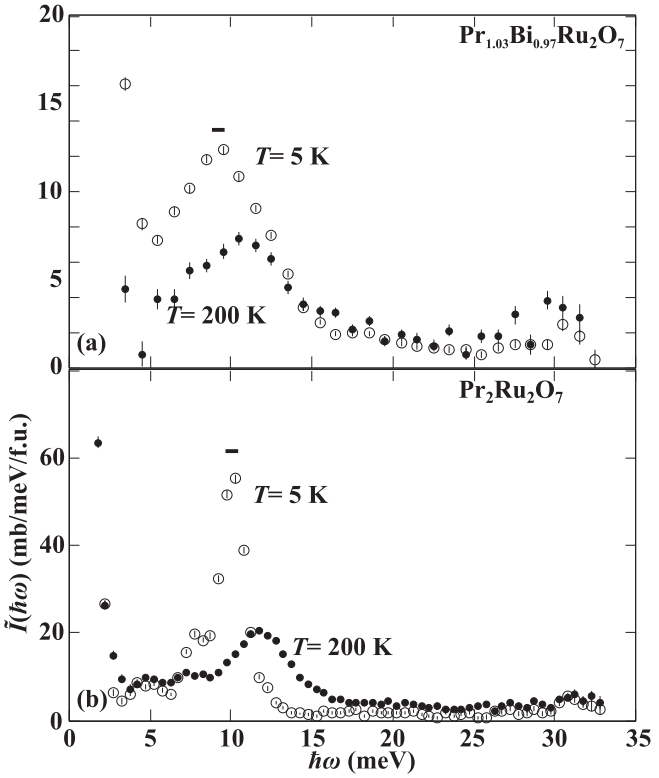

FIG. 4. The inelastic neutron scattering from $Pr_{2-x}Bi_xRu_2O_7$ for $x = 0.97$ (a) and $x = 0$ (b) at low scattering angles ($2\theta = 19^\circ$) at 5 K (○) and 200 K (●) after subtracting off the nonmagnetic phonon background. The incident energy was $E_i = 35$ meV. The horizontal bar at 10 meV indicates the instrumental resolution at that energy transfer.

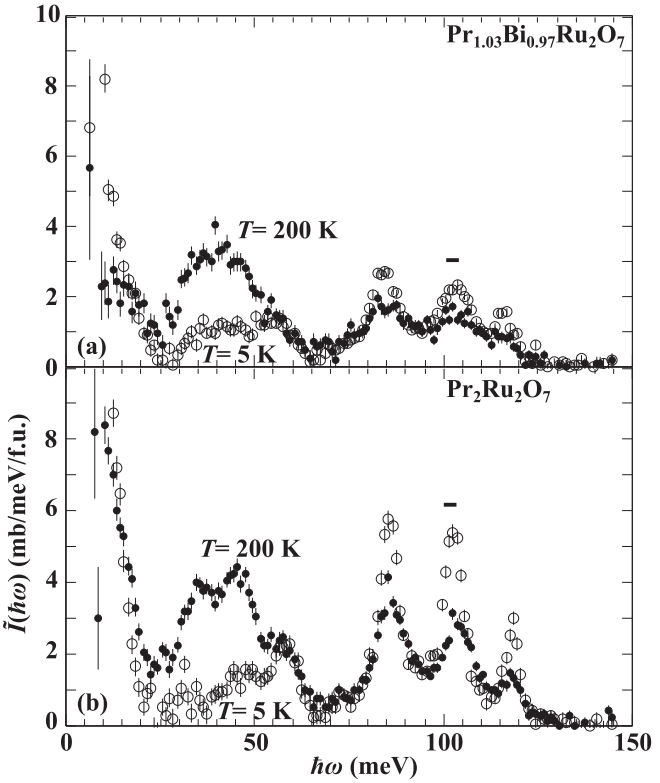

FIG. 5. The inelastic neutron scattering from $Pr_{2-x}Bi_xRu_2O_7$ for $x = 0.97$ (a) and $x = 0$ (b) at low scattering angles ($2\theta = 19^\circ$) at 5 K (○) and 200 K (●) after subtracting off the nonmagnetic phonon background. The incident energy was $E_i = 160$ meV. The horizontal bar at 105 meV indicates the instrumental resolution at that energy transfer.

200 K. A direct subtraction method was also tried, but let to similar results with increased statistical error.

The magnetic neutron scattering cross section for $Pr_2Ru_2O_7$ at 5 K shows at least five magnetic excitations centered near 10, 50, 85, 105, and 116 meV energy transfer [Figs. 4(b) and 5(b)]. Closer examination of the 5-K data shows the excitations near 10 and 50 meV are broadened or split. The remaining three high-energy excitations take the form of isolated resolution-limited peaks.

Comparing the spectrum at 200 K with that at 5 K, the following changes are observed upon warming: the strongest peak near 10 meV is broadened, decreases in intensity, and shifts upward to 12 meV. A new broad double-peak structure that resembles the broad 50 meV peak appears near 40 meV. The three peaks near 100 meV remain in place but lose intensity.

In the nominal D_{3d} point-group symmetry of the pyrochlore lattice, Pr^{3+} has five CF excitations within the ground-state $J = 4$ multiplet. The broadening and splitting of the two lowest-energy CF excitations may indicate an inhomogeneous environment for praseodymium, something we also find evidence for in high-resolution low-energy measurements that will be described subsequently. Thermal expansion as well as magnetostriction and dipole fields from Ru^{4+} ordering at $T_N = 165$ K may be responsible for the modifications in the lowest-energy CF excitations upon heating to 200 K. Anomalous changes in crystal-field excitations resulting from ruthenium spin ordering were previously documented for $Ho_2Ru_2O_7$ [33].

Thermal population of the 10-meV CF level at $T = 200$ K enables excitations from that level to higher-energy CF levels, to which dipole transitions are allowed from the excited state. Thus, heating can produce extra versions of higher excitations downshifted by ∼12 meV, which is the energy of the first excited CF state at 200 K. We interpret the heating-induced peak near 40 meV as resulting from this mechanism. This implies a finite dipole matrix element between the 12- and 50-meV CF levels. On the other hand, the loss of intensity for the three upper CF transitions indicates the dipole matrix elements between the first excited state state and these three levels is small, or even zero.

The corresponding 5-K data for the $x = 0.97$ sample also show five excitations [Figs. 4(a) and 5(a)]. We associate all of these magnetic peaks with Pr^{3+} CF excitations. As for $Pr_2Ru_2O_7$, there are four relatively sharp features centered at 9, 83, 103, and 116 meV and a broad maximum near 50 meV. The FWHM of these excitations is, however, a factor 3 larger than for $x = 0$, an effect we may ascribe to alloying induced disorder in the electrostatic conditions for Pr^{3+} [37]. The effects of heating to 200 K are very similar to observations in $Pr_2Ru_2O_7$. As the $x = 0.97$ sample has no magnetic phase transition down to 2 K, the similarity of the $x = 0$ and 0.97

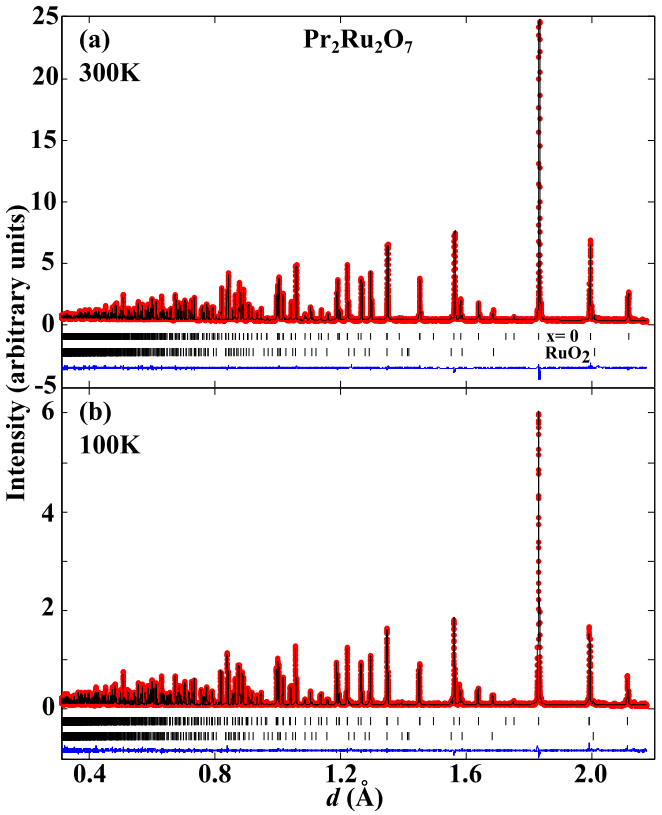

FIG. 6. Neutron powder diffraction data for $Pr_2Ru_2O_7$ ($x = 0$) at 300 K (a) and 100 K (b) collected on HRPD. The solid black line shows the Rietveld fit to the data, the residual of the fit (blue line) is shown at the bottom of the plot. The upper and lower tick marks indicate Bragg reflections from the crystal structure of the $x = 0$ and RuO_2 impurity phase, respectively.

data suggests ruthenium magnetic ordering does not have a significant effect on praseodymium here.

C. Neutron powder diffraction measurements

To determine the magnetic ordering and potential structural distortions in $Pr_2Ru_2O_7$, we carried out neutron diffraction measurements on BT1 at NIST and HRPD at ISIS. Figure 6 shows the Rietveld fits to the 300-K ($T > T_N$) and 100-K ($T < T_N$) data sets as collected on HRPD. These fits show that $Pr_2Ru_2O_7$ adopts the cubic pyrochlore structure and that the sample contained 3.46 wt. % unreacted RuO_2. Fits of the crystal structure to the data collected below T_N revealed no evidence, within the accuracy of the experiment, of a structural distortion associated with the magnetic phase transition.

Figure 7 shows Rietveld fits to the low-angle part of the neutron powder diffraction profile for $x = 0$ measured above and below T_N. It is clear that for $T < T_N$ there is additional intensity associated with the (111) and (220) reflections that can not be accounted for by nuclear contributions only (Table I). As the second phase RuO_2 is a Pauli paramagnet, this additional intensity must be due to long-range ordering of Ru dipole moments in $Pr_2Ru_2O_7$. The enhanced (111) and (222) magnetic scattering resembles our results for $Y_2Ru_2O_7$, but differs from the structures observed in $Ho_2Ru_2O_7$ and

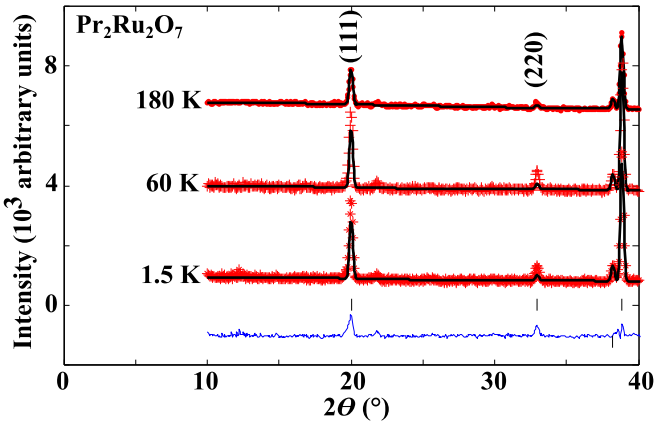

FIG. 7. Low-angle part of the neutron powder diffraction profile of $Pr_2Ru_2O_7$ as measured at 180 K (•), 60 K (+), and 1.5 K (*) on BT1. The solid black lines show the Rietveld fit of the crystal structure (Table I) to the data, the residual of the 1.5-K fit (blue line) is shown at the bottom of the plot. The tick marks shown indicate Bragg reflections coming from the crystal structure of the $x = 0$ phase.

$Er_2Ru_2O_7$ [31,33,34]. Down to 1.5 K, we did not detect additional intensity that might be associated with ordering and/or freezing of the Pr sublattice. This is consistent with our heat-capacity measurements, which show there is no additional phase transition in the relevant low-temperature range (Fig. 8). The low-T upturn in the specific heat is a nuclear Schottky anomaly associated with the nuclear spin-$\frac{5}{2}$ of ^{141}Pr [58].

D. Low-energy excitations

To better understand the rare-earth magnetism in $Pr_{2-x}Bi_xRu_2O_7$ we carried out low-energy inelastic neutron scattering measurements on $Pr_2Ru_2O_7$ using the IRIS spectrometer. Figure 9 shows inelastic neutron scattering at 1.5, 13, and 100 K ($T < T_N$) and 200 K ($T > T_N$). At 1.5 K, a sharp mode centered at ~0.25 meV is observed. At this temperature the magnetic moments on the Ru sublattice are ordered and all the CF excitations are accounted for at higher energies. The

TABLE I. Refined structural parameters from fits to powder neutron diffraction profiles of the $x = 0$ sample, collected at 180, 60, and 1.5 K on BT1. The crystal structure is cubic with space group $Fd\bar{3}m$, with Pr located on 16(d) sites (1/2,1/2,1/2), Ru located on 16(c) sites (0,0,0), and O located on 48(f) (O1) and 8(b) (O2) sites (x,1/8,1/8) and (3/8,3/8,3/8), respectively.

T (K)	180	60	1.5
a (Å)	10.36494(5)	10.36048(4)	10.36031(4)
x_{O1}	0.32919(8)	0.32932(7)	0.32929(6)
$\langle u^2\rangle$(Pr) (Å^2)	0.0094(5)	0.0076(5)	0.0075(5)
$\langle u^2\rangle$(Ru) (Å^2)	0.0032(4)	0.0027(4)	0.0027(3)
$\langle u^2\rangle$(O1) (Å^2)	0.0047(3)	0.0046(3)	0.0048(3)
$\langle u^2\rangle$(O2) (Å^2)	0.0047(6)	0.0044(5)	0.0041(5)
R_{wp} (%)	10.9	9.55	9.14
χ^2	1.90	2.38	2.19

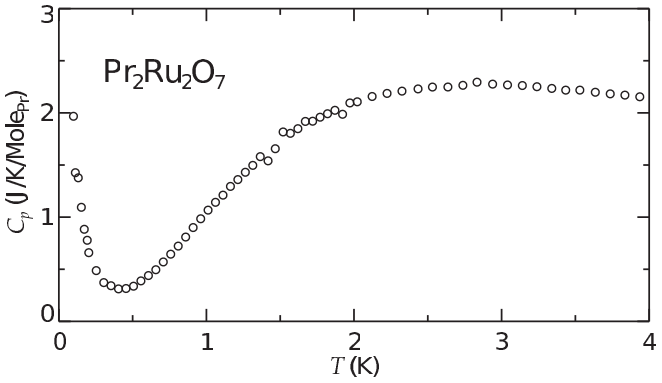

FIG. 8. Specific-heat capacity of $Pr_2Ru_2O_7$ per mole of Pr.

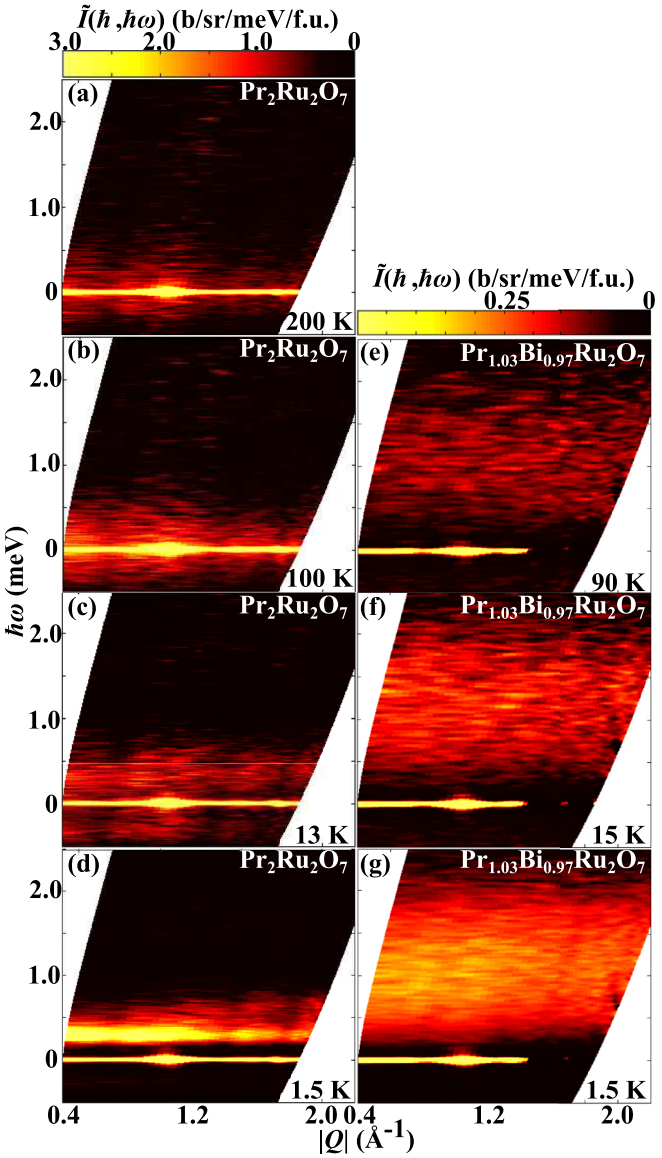

FIG. 9. Normalized inelastic neutron scattering $\tilde{I}(Q,\hbar\omega)$ for $Pr_{2-x}Bi_xRu_2O_7$ with $x = 0$ [at 200 K (a), 100 K (b), 13 K (c), and 1.5 K (d)] and for $x = 0.97$ [at 90 K (a), 15 K (b), and 1.5 K (c)] [37].

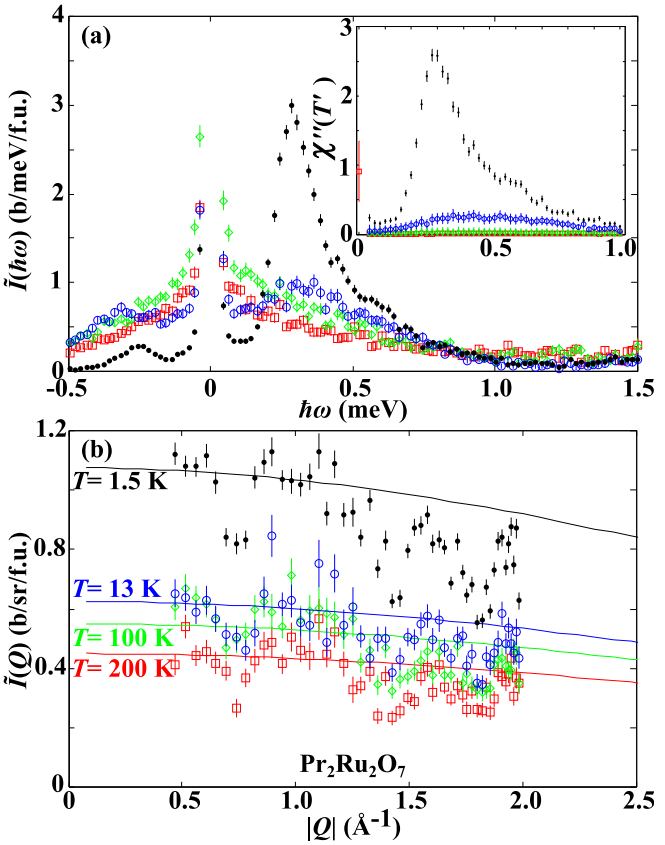

FIG. 10. Low-energy Q integrated (a) and $\hbar\omega$-integrated (b) inelastic neutron scattering intensity of $x = 0$ at 1.5 K (•), 13 K (○), 100 (◇), and 200 K (□). Data were obtained by integrating the spectra shown in Fig. 9 over the range $0.5 \leqslant |Q| \leqslant 1.5$ Å^{-1} and $0.1 \leqslant \hbar\omega \leqslant 1.0$ meV, respectively. The dips observed (at all temperatures) at 0.7 Å^{-1}, ∼1.4 Å^{-1}, and ∼1.8 Å^{-1} in (b) are due to variations in detector channel sensitivity (see text for more details). The solid lines shows $|F(Q)|^2$ calculated for Pr^{3+} scaled to the data. Inset shows the same data as in (a) multiplied by $(1 - e^{-\beta\hbar\omega})$ which, according to the fluctuation theorem, converts it into the imaginary part of the spin susceptibility [51].

absence of any dispersion and indeed of any apparent wave-vector dependence to the scattering cross section, beyond that expected from the magnetic form factor of the praseodymium ion [Fig. 10(b)], indicate this mode is a single-ion property. Even a local cluster excitation within the frustrated spin system (zero-energy mode) is not viable as that would result in Q-dependent intensity from the cluster structure factor.

It is interesting then that the Q-integrated local spectrum is not resolution limited, but has a certain line shape that changes with temperature [Fig. 10(a)]. This is unlike what is observed for the $x = 0.97$ sample [37]. Apart from an overall decrease in intensity with increasing temperature, the Q dependence of the scattering [Fig. 10(b)] follows the single-ion form factor at all temperatures. The dips observed (at all temperatures) at 0.7 Å^{-1}, ∼1.4 Å^{-1}, and ∼1.8 Å^{-1} coincide with dips in the nuclear incoherent elastic scattering for the same detectors. Thus, these sharp modulations are extrinsic and may be due to variations in detector channel sensitivity

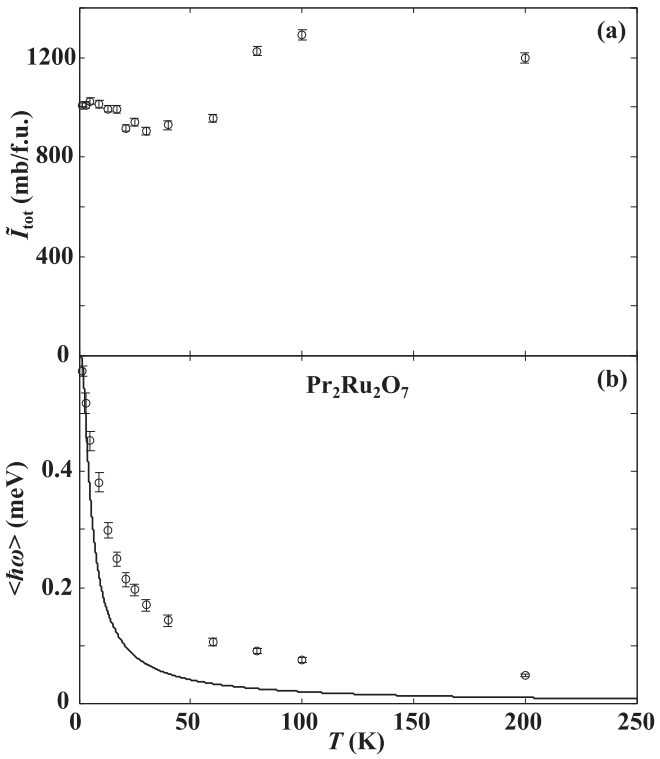

FIG. 11. Temperature dependence of the integrated intensity (a) and average energy (b) as defined in Eq. (7) of the low-energy magnetic neutron scattering from $Pr_2Ru_2O_7$. The region of integration covers $0.5 \leqslant |Q| \leqslant 1.75$ Å^{-1} and $0.1 \leqslant \hbar\omega \leqslant 2.75$ meV. The solid line in (b) is given by Eq. (8) with $\Delta = 0.6$ meV.

during the measurements. While the absence of intrinsic Q dependence beyond that of the form factor indicates short-range correlations and the importance of single-ion physics, the temperature-dependent spectrum is inconsistent with a pure single-ion effect for $x = 0$.

To summarize and interpret the inelastic magnetic scattering we plot the temperature dependence of the zero- and first-energy moments of the spectrum [59]:

$$\tilde{I}_{\rm tot} = \int_{-\infty}^{\infty} \tilde{I}(\hbar\omega)\hbar\, d\omega \approx \int_{\epsilon}^{E_{\rm max}} (1 + e^{-\beta\hbar\omega})\tilde{I}(\hbar\omega)\hbar\, d\omega, \quad (6)$$

$$\langle\hbar\omega\rangle = \frac{\int_{-\infty}^{\infty} \hbar\omega\tilde{I}(\hbar\omega)d\omega}{\int_{-\infty}^{\infty} \tilde{I}(\hbar\omega)d\omega} \approx \frac{\int_{\epsilon}^{E_{\rm max}} \hbar\omega(1 - e^{-\beta\hbar\omega})\tilde{I}(\hbar\omega)d\omega}{\int_{\epsilon}^{E_{\rm max}} (1 + e^{-\beta\hbar\omega})\tilde{I}(\hbar\omega)d\omega}. \quad (7)$$

Here, we have employed detailed balance: $\tilde{I}(-\hbar\omega) = \exp(-\beta\hbar\omega)\tilde{I}(\hbar\omega)$, $\epsilon = 0.1$ meV is a lower cutoff necessitated by the strong incoherent elastic nuclear scattering, while $E_{\rm max} = 2.75$ meV is the upper cutoff in the integration. The result is shown in Fig. 11, if $\epsilon = 0$ and $E_{\rm max}$ were sufficiently large the total moment sum rule ensures that $I_{\rm tot}$ should be T independent. The drop observed in $I_{\rm tot}$ below 100 K indicates that magnetic scattering is shifting out of the range of integration at the magnetic phase transition. Specifically, quasielastic magnetic scattering from ruthenium is shifting into the elastic line in the form of Bragg peaks, which our $\epsilon = 0.1$ meV lower cutoff exclude from $I_{\rm tot}$. It is easy to show the following expression for Eq. (7) holds when the level scheme consists of a single excited state at an energy Δ above the ground state:

$$\langle\hbar\omega\rangle = \Delta \tanh\left(\frac{\beta\Delta}{2}\right). \quad (8)$$

This functional form is not consistent with the data shown in Fig. 11(b). In particular, the decrease in $\langle\hbar\omega\rangle$ observed upon heating $Pr_2Ru_2O_7$ is not as pronounced as would be expected based on a temperature-independent spectrum. This implies an upward renormalization of the first moment $\langle\hbar\omega\rangle$ upon heating. An upward shift of the characteristic energy with T is indeed directly visible in the inset to Fig. 10(a). While the origin of this effect is presently not clear, we remark that it goes beyond a simple rigid crystal-field effect and is expected for quantum spin systems with a collective energy gap on general grounds. The Haldane spin chain offers a specific example where this effect has been observed and can be understood as a result of thermally induced magnon confinement [60].

IV. ANALYSIS AND DISCUSSION

A. Local structure

To obtain quantitative information on the extent of local structural distortions, we have fitted the low-temperature EXAFS data using theoretical functions for each atom-pair, calculated using FEFF8.2 [57]. The undistorted local structure is shown in Fig. 1. In such fits, the pair distance and broadening of the pair distribution function σ are varied for distinct atomic pairs. The coordination number is obtained from the known pyrochlore structure and diffraction results. In addition, the edge energy is varied slightly to correspond to the point on the edge at which the photoelectron wave number k is zero for the theoretical functions. Also, the overall amplitude NS_o^2 (N is the coordination number) was initially allowed to vary, to determine the parameter S_o^2. This parameter takes into account multiple scattering contributions to the edge height and is typically between 0.7 and 1.0. In our analysis, we obtain an average value for S_o^2 from fits to a number of low-temperature scans: Ru K, $S_o^2 = 0.87$; Pr $L_{\rm III}$, $S_o^2 = 0.99$; and Bi $L_{\rm III}$, $S_o^2 = 1.0$. For fits at higher T, S_o^2 is kept constant. Because of the large positive correlation between S_o^2 and σ^2, there could be a significant systematic error in this parameter. We have used the above values of S_o^2 for a given edge (and all samples), for comparison purposes.

In most of the following fits we focus primarily on the nearest-neighbor metal-O peaks. However, for the pure $x = 0$ sample, detailed fitting out to ~4 Å is possible for both the Ru and the Pr $L_{\rm III}$ edges; we show an example for Pr shortly.

First, we discuss the Ru K-edge analysis; in Figs. 12(a)–12(c), we compare the fits for the Ru-O1 peak in the Ru data collected for $x = 0$, 0.97, and 2. The fit range used was 1.3–2 Å, but a good fit extends below 1 Å. Above ~2 Å the tails of higher peaks partially interfere destructively with the Ru-O

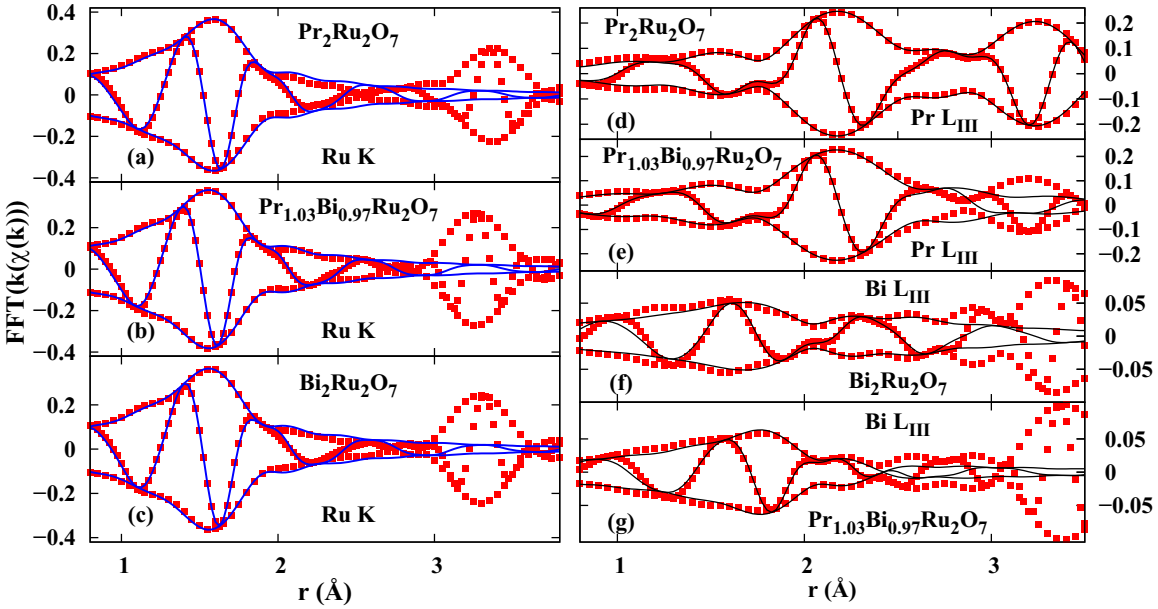

FIG. 12. Fits of the $T = 4$ K EXAFS data. (a)–(c) Ru K edge; (d), (e), Pr L_{III} edge; (f), (g), Bi L_{III} edge. Note the difference in vertical scales. For the pure sample $Pr_2Ru_2O_7$, fits beyond 4 Å are possible for both edges; an example is shown for Pr L_{III} in (d). For samples containing Bi, distortions are present and only the first metal-O peaks are fit.

peak, but the agreement is still quite good. In each case, the Ru-O1 peak is large, indicating a well-ordered structure, and the Ru-O1 bond length agrees with diffraction to better than 0.01 Å and is not tabulated. The values of σ^2 for the Ru-O1 pair at 4 K are given in Table II, and are indistinguishable for the three samples within our errors. However, the further neighbor peak near 3.3 Å changes from sample to sample; the amplitude grows as the Bi concentration increases, most likely as a result of a change in photoelectron interference. For $x = 0$, the Ru-Ru and Ru-Pr peaks are partially out of phase leading to a reduced amplitude; in $x = 0.97$, the Ru-Pr amplitude is reduced by ∼50% (and the Ru-Bi pair distribution is disordered), and hence there is less destructive interference. Because there is a changing mixture of Ru-Ru, Ru-Pr, and Ru-Bi pairs with increasing Bi concentrations, a more quantitative characterization of the disorder in the metal-metal peaks requires a more detailed fit, which is beyond the scope of this paper.

For the Pr L_{III} edge we show a detailed fit out to ∼4 Å in Fig. 12(d) for the pure $x = 0$ sample. This fit of the 4-K data includes Pr-O1, Pr-O2, the first metal-metal pairs (Pr-Pr and Pr-Ru), longer Pr-O pairs, and multiscattering peaks; the fit beyond 4 Å is poor because longer Pr-O, Pr-Pr, Pr-Ru, and multiscattering peaks are not included. We initially constrained the distances to be consistent with the crystal structure (allowing for an overall expansion of the unit cell) and used the coordination numbers from the structure to reduce the errors in σ^2. We obtained a very good fit out to 3.8 Å, with pair distances that are consistent with diffraction results.

For the mixed sample, we only fit the Pr-O peak as shown in Fig. 12(e). The amplitude of this peak is comparable to that for the pure $x = 0$ sample: the widths change slightly (see Table II for the parameters of the first two O shells for both

TABLE II. Results of analysis of EXAFS data for $Pr_{2-x}Bi_xRu_2O_7$ probing nearest-neighbor atomic pairs. A-site: Pr-O and Bi-O peaks from fits for the Pr and Bi L_{III} edges of $x = 0$, 0.97, and 2. The fit ranges for the Pr L_{III} edge are $x = 0$, 1.8–3.8 Å, and $x = 0.97$, 1.6–2.5 Å (Pr-O1 and Pr-O2 peaks only). The ranges for the Bi fits (O1 and O2 shells only) are $x = 2$, 1.2–2.8 Å, and $x = 0.97$, 1–2.4 Å. B-site: Ru-O1 peak in Ru K-edge data for for $x = 0$, 0.97, and 2; fit range 1.3–2 Å. Estimated systematic errors on r are ±0.01 Å; estimated relative errors for σ^2, ±0.0004 Å^2. The diffraction results in last column are from this work for $x = 0$ and 0.97, assuming the ideal pyrochlore structure, and from Avdeev *et al.* [38] (model h with an average position for O2) for $x = 2$. The Bi off-center displacement D for $x = 2$ is 0.16 ± 0.02 Å which is identical, within our errors, to the diffraction results of Avdeev *et al.* [38] and also agrees with Shoemaker *et al.* [43]; for $x = 0.97$, $D = 0.17 \pm 0.02$ Å.

$Pr_{2-x}Bi_x$ Ru_2O_7	Atom pair	σ^2 (Å^2)	r (EXAFS) (Å)	r (diffraction) (Å)
$x = 0$	Pr-O2	0.0060(4)	2.254(3)	2.243482(9)
$x = 0$	Pr-O1	0.0037(4)	2.558(2)	2.5453(1)
$x = 0.97$	Pr-O2	0.0062(4)	2.25(1)	2.23620(1)
$x = 0.97$	Pr-O1	0.0024(4)	2.55(1)	2.5496(4)
$x = 0.97$	Bi-O2	0.0025(4)	2.23(1)	2.23620(1)
$x = 0.97$	Bi-O1a	0.015(1)	2.44(2)	,,
$x = 0.97$	Bi-O1b	0.0046(4)	2.59(2)	2.5496(4)
$x = 0.97$	Bi-O1c	0.013(1)	2.74(2)	,,
$x = 2$	Bi-O2	0.0050(4)	2.23(1)	2.234
$x = 2$	Bi-O1a	0.0019(4)	2.37(2)	2.410
$x = 2$	Bi-O1b	0.0019(4)	2.51(2)	2.554
$x = 2$	Bi-O1c	0.0058(4)	2.65(2)	2.690
$x = 0$	Ru-O1	0.0026(2)	2.010(2)	2.0083(1)
$x = 0.97$	Ru-O1	0.0022(3)	1.999(3)	1.9944(2)
$x = 2$	Ru-O1	0.0022(3)	1.989(1)	1.989

samples). This shows that the disorder of the Pr-O1 and Pr-O2 bond lengths in the mixed sample ($x = 0.97$) are comparable to those in the pure Pr sample ($x = 0$). However, in each case, σ^2 for Pr-O2 is significantly larger than the value for Pr-O1, suggesting some disorder along the Pr-O2 axis; we return to this issue later. Also note the much smaller amplitude for the second main peak (a sum of Pr-Pr, Pr-Ru, and Pr-Bi) for the mixed sample near 3.2 Å.

For the Bi edge, the data and simulations presented in Figs. 2(b) and 2(f) show considerable disorder of the Bi-O1 shell. Since the Pr-O1 and Ru-O1 pair distributions are ordered as discussed above, this indicates that the disorder for Bi-O1 arises from displacements of Bi from the ordered A-site position, either away from or towards the ring of O1 atoms, i.e., in a direction perpendicular to the Bi-O2 axis in the Bi_4O2 tetrahedra (see Fig. 1 for the A-site tetrahedra). There may also be small, correlated, translation-rotations of the A-tetrahedra containing the Bi which could be accommodated by changes in the Pr-O1-Ru angles with little disorder of the Ru-O1 and Pr-O1 bonds, consistent with the Pr and Ru EXAFS discussed above.

Diffraction studies find a displacement of Bi away from the Bi-O2 axis in the end compound $x = 2$, and attributed it to the $6s$ lone pair electrons on Bi^{3+} [38]. The distortion has been modeled by allowing the Bi to move off center a distance D in six equivalent directions and then setting the filling fraction at $\frac{1}{6}$. For example, one direction for Bi to move off center is towards a Ru atom, or midway between two O1 atoms (six possibilities): this is called the h model, and the site is 96h $(0, y, -y)$ in space group $Fd\bar{3}m$. They also considered a similar model with the six off-center directions rotated by $\sim 30^\circ$, i.e., approximately displaced towards the midpoint between two Ru atoms or roughly towards an O1 atom: this is called the g model; site 96g (x,x,z). For this model, the off-center displacements are not quite perpendicular to the undistorted Bi-O2 axis and the ring of displaced sites is slightly corrugated. In our first fits we tried just a broad distribution for Bi-O1. These do not fit well and discrete Bi-O1 distances are required as indicated in the diffraction studies.

The diffraction results also suggest that the O2 atoms are displaced along four symmetry directions (with occupancy $\frac{1}{4}$ for each off-center site) [38]. Assuming that the Bi and O2 off-center displacements are uncorrelated, this leads to a very broad distribution of Bi-O2. We have tried this distribution for O2 and it does not fit our EXAFS data; although there is some broadening of the Bi-O2 distribution it is much smaller than suggested from uncorrelated displacements of Bi and O2. In the models we compare below we use a single peak for Bi-O2 but allow it to broaden slightly.

For the h model there are three Bi-O1 peaks approximately at r_0 and $r_0 \pm \delta r$ (where $\delta r \sim 0.85D$); each peak corresponds to two O1 neighbors, thus, the numbers of neighbors in the peaks are in the ratio 2:2:2 and we refer to it as the 222 model. For the g model there are four Bi-O1 distances, one O1 neighbor each at $r_0 \pm \delta r_1$ and two neighbors each at $r_0 \pm \delta r_2$; we therefore call this model the 1221 model (the ratio of the O1 coordinations). In fitting the O peak one needs to remember that when there are two quite close bond lengths (here the Bi-O1 and Bi-O2, or Pr-O1 and Pr-O2) then there will be interference between the two components in r space. The dip at 1.7–1.8 Å for the Pr data and near 2.1 Å for the Bi data are the results of this interference.

We have carried out fits using both the 222 and 1221 models described above (h and g models in diffraction). The fits were similar, with the h model slightly better; however, the improvement in the goodness of fit parameter was not statistically significant, based on the Hamilton F test [61]; thus, Bi-O1 can be quite well modeled using either distribution. However, Shoemaker *et al.* [43] also find that the h model is better from nuclear density plots for $x = 2$. Consequently, we only show results for this model. In Fig. 12(f) we show the fits of the Bi-O peak for $x = 2$ and in Fig. 12(g) the fit for the mixed compound $x = 0.97$. The fit ranges are 1.2–2.8 and 1.0–2.4 Å, respectively. The data and fits show that for the shorter Bi-O2 peak, the pure compound ($x = 2$) is slightly more disordered than the alloy ($x = 0.97$). In contrast for the Bi-O1 peak, the amplitude from 2–2.8 Å is lower for the mixed compound indicating more disorder of the Bi-O1 pair in this material, which for the split peak model requires a larger broadening of the three individual split Bi-O1 peaks. Surprisingly, the Bi off-center displacement D that leads to this splitting for the mixed sample is about the same, 0.17 Å within our uncertainty, ±0.02 Å, as for the $x = 2$ sample. Some parameters are provided in Table II; note $D \sim \delta r/0.85$ for the h model.

Comparing the mean-squared atomic displacements obtained from the fits to the neutron diffraction data (Table I), with the σ^2 values obtained for Ru-O1, Pr-O1, and Pr-O2 (0.0027, 0.0033, and 0.0058 $Å^2$, respectively) obtained from our EXAFS analysis (Table II) for $x = 0$, we can observe the following. The disorder in the Ru-O1 and Pr-O1 bonds is very small while that for Pr-O2 is about twice as large; also, the ratio of the $\langle u^2 \rangle$ parameters for Pr and the O1/O2 atoms is close to 2. This indicates that the O1 atoms have little disorder. The three large quantities are $\langle u^2 \rangle$ for Pr and σ^2_{static} for Pr-O2 and Pr-Pr. If Pr is displaced a little along the Pr-O2 axis, it will only affect σ^2 for the Pr-O2 and Pr-Pr pairs, and Pr $\langle u^2 \rangle$ parameters. This suggests that there is some intrinsic disorder on the Pr site in the pyrochlore structure which could be the origin of the inhomogeneous splitting of the nominal non-Kramers crystal-field doublet.

To further explore possible disorder on the Pr site we carried out a temperature-dependent EXAFS study at the Pr L_{III} edge. The temperature dependence of the Debye-Waller factor $\sigma^2(T)$ provides an estimate of the zero-point motion (ZPM) contribution, σ^2_{ZPM}, to σ^2 at low T; if there is significant static disorder, $\sigma^2(4\text{ K})$ will exceed the value associated with zero-point motion. Subtracting in quadrature, we obtain the contribution from static disorder: $\sigma_{\text{static}} = \sqrt{\sigma^2(4\text{ K}) - \sigma^2_{\text{ZPM}}}$. In Fig. 13 we plot $\sigma^2(T)$ for the Pr-O1, Pr-O2, Pr-Ru, and Pr-Pr pairs. It is important to remember that for EXAFS, σ^2_{ZPM} depends on the reduced mass of the pair of atoms, and the value of $\sigma^2(4\text{ K})$ for both Pr-O1 and Pr-Ru are both very close to the value for ZPM. The solid lines are fits to a correlated Debye model [56,62,63]. The Pr-O2 pair is a much stiffer bond (low slope) but σ^2 at low T is large, $\sim 0.0058\ Å^2$, indicating a significant static contribution. A similar behavior is observed when comparing the Pr-Ru and Pr-Pr pairs which have the same pair distance. The Pr-Ru pair has little static disorder at

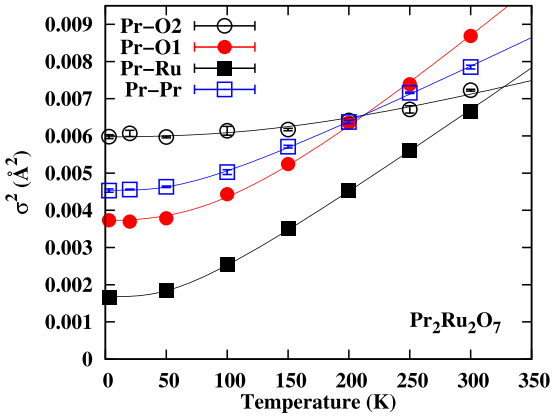

FIG. 13. Plots of σ^2 vs T for the Pr-O1, Pr-O2, Pr-Ru, and Pr-Pr pairs in $Pr_2Ru_2O_7$ from EXAFS data at the Pr L_{III} edge. The value of σ^2 for the Pr-O2 pair at low T is large (~0.0058 Å^2) compared to the Pr-O1 pair, indicating a significant static contribution. A similar behavior is observed when comparing the Pr-Ru and Pr-Pr pairs; σ^2 for the Pr-Pr pair (~0.0043 Å^2) is significantly larger than the value for the Pr-Ru pair at 4 K, again indicating a significant static contribution to the peak broadening. The solid lines are fits to a correlated Debye model. The correlated Debye temperatures are Pr-O1: 520(30) K; Pr-O2: 880(50) K; Pr-Ru: 290(5) K; Pr-Pr: 316(5) K. Relative errors are indicated by parentheses; absolute errors, mainly from systematic effects are ~10%. The static offsets σ^2_{static} for Pr-O2 and Pr-Pr from the fits are 0.0036(6) and 0.0029(6) Å^2, respectively, while the corresponding values for Pr-O1 and Pr-Ru are close to zero (<0.0004 Å^2).

low T while σ^2 for the Pr-Pr pair is large at 4 K (0.0043 Å^2) indicating a large static contribution (see caption of Fig. 13 for more information). The low static disorder for Pr-O1, Pr-Ru, and previously for the Ru-O1 pair, suggests the disorder is primarily along the Pr-O2 axis. Since $\langle u^2 \rangle$ for O1 and O2 are comparable and much smaller than $\langle u^2 \rangle$ for Pr (Table I), most of the disorder must be about the Pr site. Assuming a Pr displacement along the Pr-O2 axis, the magnitude is $\sigma_{static} \sim$ 0.05–0.06 Å.

B. Single-ion properties

To understand the observed local low-energy spin excitations in $Pr_{2-x}Bi_xRu_2O_7$ near the metal-to-insulator transition, it is important to determine the relevant low-energy spin degrees of freedom in this system [37]. For this we have analyzed the high-energy magnetic neutron scattering from $x = 0.97$, $x = 0$ (Figs. 4 and 5) to determine the ground-state and CF levels of Pr. Our preliminary analysis in Sec. III B identified five CF excitations, consistent with Pr^{3+} being in a CF approximating D_{3d} symmetry for which the CF Hamiltonian is given by Eq. (2). Neutron scattering theory allows us to express the dynamic spin correlation function corresponding to a transition from the CF state $|p\rangle$ to $|q\rangle$ as follows [51]:

$$S^{\alpha\alpha}(\mathbf{Q},\omega) = \sum_{\alpha} \sum_{p,q} \frac{2}{3} \rho_p |\langle p|J^{\alpha}|q\rangle|^2 \delta(E_p - E_q + \hbar\omega), \quad (9)$$

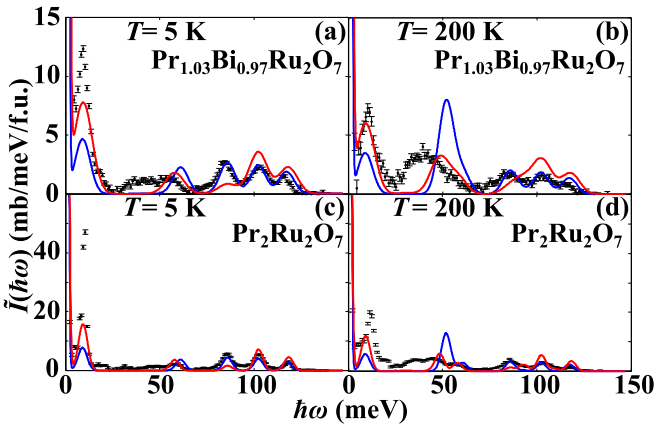

FIG. 14. Combined $E_i = 35$ and 160 meV magnetic scattering from $Pr_{2-x}Bi_xRu_2O_7$ for $x = 0.97$ and 0 at 5 K (a), (c) and 200 K (b), (d) (•). The solid lines show the calculated spectra for Model 1 (blue line) and Model 2 (red line) using the fitted CF parameters listed in Table III, including an intrinsic Gaussian broadening of the transitions. Only this intrinsic Gaussian broadening has been allowed to vary between $x = 0.97$ and 0.

where ρ_p is the occupancy of the state $|p\rangle$ with energy E_p. A Monte Carlo search of the CF parameter space was performed to obtain an initial set of CF parameters used to fit the data. For the Monte Carlo search and the fitting of the CF parameters, the spectra with incident energies $E_i = 35$ and 160 meV were combined into one spectrum (Fig. 14). Problems arose during the analysis of the CF excitations due to the additional broadening of the CF level excitation at around 50 meV compared to the other CF level excitations, which cannot be accounted for by the single-ion CF Hamiltonian given in Eq. (2). Interactions with conduction electrons and magnetoelastic coupling are possible origins of this broadening.

While phonons and CF excitations may be considered independent by approximation, coupling between the two types of excitations is inevitably a factor. Magnetoelastic effects have previously been documented for $CeCu_2$, $YbPO_4$, and $CeCuAl_3$ [64–68]. The effect is broadening or even over damping of energy levels that cannot be explained by the simple single-ion CF model. CF excitations are also sensitive to local disorder, which influences the electrostatic environment surrounding the magnetic ion.

Figure 3 shows the 50-meV CF excitation overlaps with phonon scattering that is visible at low scattering angles due to multiple scattering. This is not the case for the other CF excitations. It is not unreasonable to assume that the broadening which is observed in these two materials for the 50-meV CF excitation is due to magnetoelastic coupling. Additional (single-crystal inelastic neutron scattering and Raman scattering) experiments are needed to determine whether or not this hypothesis is correct. In the following analysis of the high-energy magnetic excitations, the possibility of CF phonon coupling has not been taken into account and the single-ion CF Hamiltonian [Eq. (2)] was employed. Disorder-related broadening is observed for all CF level excitations in $Pr_{2-x}Bi_xRu_2O_7$ for $x = 0.97$, which are much broader than for $x = 0$.

TABLE III. Fitted CF parameters of $Pr_{2-x}Bi_xRu_2O_7$ for $x = 0$. The parameters were obtained from fits to the magnetic excitation spectrum at 5 K. All parameters are in meV.

	Model 1	Model 2
B_2^0	$-8(1) \times 10^{-1}$	$-1.3(2)$
B_4^0	$-4.2(5) \times 10^{-2}$	$-2(1) \times 10^{-3}$
B_4^3	$2.9(3) \times 10^{-1}$	$6.4(8) \times 10^{-1}$
B_6^0	$7.7(2) \times 10^{-4}$	$8.3(3) \times 10^{-4}$
B_6^3	$3(3) \times 10^{-3}$	$1.09(6) \times 10^{-2}$
B_6^6	$4.1(8) \times 10^{-3}$	$6(1) \times 10^{-3}$

The Monte Carlo search of the parameter space identified two sets of CF parameters consistent with the observed excitation spectrum. These two sets of CF parameters were used as the starting point for a fit to the 5-K spectrum of the pure material, allowing for an intrinsic Gaussian broadening of all transitions. Both models yield similar fits to the data. The refined values of the individual CF parameters for both models are listed in Table III, while the corresponding energy levels and eigenvectors are given in Table IV. The latter table shows that the two models have similar ground states, but different excited states. Model 1 has a doublet ground state, followed by a singlet, a doublet, two singlets, and a doublet, while Model 2 has a doublet ground state, followed by three singlets and two doublets. Both models have a doublet ground state and a singlet first excited state and the symmetry of these two states is the same in both models. The inference that the Pr ions have a doublet ground state is consistent with the observation of a low-energy magnetic excitation, which we associated with disorder at the atomic level that lifts the D_{3d} symmetry and gives rise to a distribution of local environments and an effective random transverse field [37].

Figure 14 shows the calculated spectra for both models, compared with measurements on the pure ($x = 0$) and dilute ($x = 0.97$) material at 5 and 200 K. For the dilute material only the intrinsic Gaussian broadening was allowed to vary. At 5 K, the possibility of an internal magnetic field due to the ordering of the Ru sublattice in the pure material was not taken into account in the calculated spectra. Figure 14 shows that even though the calculated CF level energies are close to those observed in both materials, there is a large discrepancy between the observed and calculated spectra. At both 5 and 200 K, Model 1 gives a better description of the three excitations around 100-meV energy transfer than Model 2, while Model 2 gives a slightly better description of the excitation at 10 meV energy transfer. Both models have problems describing the broad excitation centered at around 50-meV energy transfer. They do have similar temperature dependencies as found experimentally. Specifically, both feature a transition from the first excited state at 10 meV to the second excited state at around 50 meV energy transfer.

While it is clear from Fig. 14 that the simple single-ion CF model does not provide an adequate description of the data and that there are additional interactions that influence the magnetic response, the analysis does indicate that the Pr ions have a non-Kramers doublet ground state. Similar results have recently been reported for $Pr_2Sn_2O_7$, $Pr_2Zr_2O_7$, and $Pr_2Hf_2O_7$ [69–72]. In all three cases it was found, from inelastic neutron scattering experiments, that a significant admixture of the higher-J multiplets into the ground-state J multiplet was needed to fit the data. This was not taken into account in our analysis. Even so, the symmetry obtained in all three systems for the ground and first excited states, without the admixture of the higher-J multiplets, is identical to that reported here. Analysis of the $Pr_2Sn_2O_7$ data also revealed that the Pr^{3+} non-Kramers doublet ground state has strong Ising-type anisotropy [69].

Magnetoelastic effects might explain the observed unequal broadening of the 50-meV level, while the additional broadening of this mode for $x = 0.97$ could be due to alloying-induced disorder.

TABLE IV. Energies (E_i in meV) and CF wave functions (ψ_i) of the ninefold-degenerate ground-state multiplet $^4H_3$ of $Pr_{2-x}Bi_xRu_2O_7$. The CF level energies and wave functions were calculated for both models using the CF parameters listed in Table III, (<) represents a CF doublet level.

E_i	Ψ_i
	Model 1
0<	$\psi_g = 0.935\|\mp4\rangle - 0.073\|\pm2\rangle \pm 0.348\|\mp1\rangle$
9.10	$\psi_1 = -0.166\|3\rangle + 0.972\|0\rangle + 0.166\|-3\rangle$
61.02<	$\psi_2 = \mp0.348\|\mp4\rangle\mp0.013\|\pm2\rangle + 0.937\|\mp1\rangle$
86.02	$\psi_3 = 0.686\|3\rangle + 0.235\|0\rangle - 0.687\|-3\rangle$
102.41	$\psi_4 = 0.707\|3\rangle + 0.707\|-3\rangle$
117.44<	$\psi_5 = 0.063\|\mp4\rangle + 0.989\|\pm2\rangle \pm 0.039\|\mp1\rangle$
	Model 2
0<	$\psi_g = 0.860\|\mp4\rangle - 0.121 \pm 2\rangle \pm 0.495\|\mp1\rangle$
9.32	$\psi_1 = -0.626\|3\rangle + 0.465\|0\rangle + 0.626\|-3\rangle$
57.92	$\psi_2 = 0.707\|3\rangle + 0.707\|-3\rangle$
86.15	$\psi_3 = 0.329\|3\rangle + 0.885\|0\rangle - 0.329\|-3\rangle$
102.49<	$\psi_4 = 0.017 \mp 4\rangle + 0.978\|\pm2\rangle \pm 0.210\|\mp1\rangle$
118.47<	$\psi_5 = \pm0.509\|\pm4\rangle \pm 0.173\|\mp2\rangle + 0.843\|\pm1\rangle$

C. Magnetic ordering

As noted in Sec. III C, cooling the $x = 0$ sample through T_N yields additional Bragg intensity that cannot be accounted for by nuclear contributions only but must come from magnetic Bragg diffraction associated with long-range magnetic ordering on the Ru sublattice. The magnetic Bragg peaks sit on top of nuclear Bragg peaks and so are indexed by a $\mathbf{k} = (0,0,0)$ propagation vector and their increase below T_N is similar to that observed for $Y_2Ru_2O_7$ [31]. Indeed, the model proposed for $Y_2Ru_2O_7$ gives a very good fit to the data for $Pr_2Ru_2O_7$ (Fig. 15). The corresponding ordered Ru moment [$1.48(4)\mu_B$] is similar to that obtained for $Y_2Ru_3O_7$ ($1.36\mu_B$). As the magnetic transition is second order we have performed representational analysis using the SARAH program to gain a more detailed understanding of the Ru magnetic ordering in $Pr_2Ru_2O_7$ [73].

1. Representational analysis

For space group $Fd\bar{3}m$ with propagation vector $\mathbf{k} = (0,0,0)$ the magnetic representation of the Ru (and Pr) sublattice

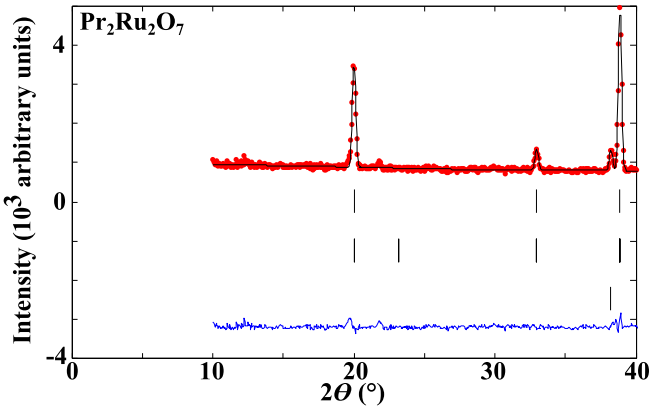

FIG. 15. Rietveld fit (solid black line) of the $Y_2Ru_2O_7$ model to the $Pr_2Ru_2O_7$ neutron powder diffraction profile measured at $T = 1.5$ K (•). The residual of the fit (blue line) is shown at the bottom of the plot [$R_p = 10.7\%$, $R_{wp} = 8.63\%$, $R_{magn} = 5.49\%$, $\chi^2 = 1.91$, μ(Ru)= 1.48(4)μ_B]. The upper, middle, and lower tick marks indicate Bragg reflections coming from the crystal, magnetic structure of the $x = 0$, and RuO_2 impurity phase, respectively.

contains the following irreducible representations (IRs) [73]:

$$\Gamma_{mag} = \Gamma_3^1 + \Gamma_6^2 + \Gamma_8^3 + 2\Gamma_{10}^3. \quad (10)$$

The corresponding basis vectors (BVs) are listed in Table V. We have fitted each IR to the neutron diffraction profiles collected at 1.5 and 60 K. This was done to look for evidence of possible Pr ordering at low temperatures. It was found for all IRs that adding an ordered moment on the Pr sublattice does not significantly improve the fit. The corresponding limit of $\sim 0.3\mu_B$ imposed on the ordered Pr moment is much lower than the saturated $1.56\mu_B$ moment of the doublet ground state. Allowing for different IRs for Ru and Pr ordering yields a similar upper bound on any ordered dipole moment on the Pr site. The fits to the 1.5-K data, listed in Table VI, shown in Fig. 16, and discussed below, therefore only take into account an ordered moment on the Ru sublattice and it appears that the ground state of praseodymium in these compounds is a quadrupolar singlet.

TABLE V. Basis vectors for the irreducible representations given in Eq. (10) [73]. The Ru/Pr atoms of the nonprimitive basis are defined according to 1: (0, 0, 0)/(0.5, 0.5, 0.5), 2: (0.5, 0.75, 0.25)/(0, 0.25, 0.75), 3: (0.25, 0.5, 0.75)/(0.75, 0, 0.25), and 4: (0.75, 0.25, 0.5)/(0.25, 0.75, 0).

		BV components											
		Atom 1			Atom 2			Atom 3			Atom 4		
IR	BV	m_a	m_b	m_c	m_a	m_b	m_c	m_a	m_b	m_c	m_a	m_b	m_c
Γ_3	ψ_1	1	1	1	−1	−1	1	−1	1	−1	1	−1	−1
Γ_6	ψ_2	2	−1	−1	−2	1	−1	−2	−1	1	2	1	1
	ψ_3	0	−1	1	0	1	1	0	−1	−1	0	1	−1
Γ_8	ψ_4	1	−1	0	−1	1	0	1	1	0	−1	−1	0
	ψ_5	0	1	−1	0	1	1	0	−1	−1	0	−1	1
	ψ_6	−1	0	1	−1	0	−1	1	0	−1	1	0	1
Γ_{10}	ψ_7	1	1	0	−1	−1	0	1	−1	0	−1	1	0
	ψ_8	0	0	1	0	0	1	0	0	1	0	0	1
	ψ_9	0	1	1	0	1	−1	0	−1	1	0	−1	−1
	ψ_{10}	1	0	0	1	0	0	1	0	0	1	0	0
	ψ_{11}	1	0	1	1	0	−1	−1	0	−1	−1	0	1
	ψ_{12}	0	1	0	0	1	0	0	1	0	0	1	0

TABLE VI. Refined magnetic parameters from fits of the individual IRs given in Eq. (10) to powder neutron diffraction profiles of the $x = 0$ sample collected at $T = 1.5$ K. For the fits of Γ_8 to the data, the size of the ordered moment was fixed to $1.41\mu_B$. For Γ_8 and Γ_{10} only ψ_4 and $\psi_7 + \psi_8$, respectively, were fitted to the data as the other associated BVs are related by alternative choice of lattice axis.

IR	Γ_3	Γ_6		Γ_8	Γ_{10}
BV	ψ_1	ψ_2	ψ_3	ψ_4	$\psi_7 + \psi_8$
R_p (%)	11.1	10.7	10.7	11.2	11.0
R_{wp} (%)	8.94	8.62	8.62	9.21	8.84
R_{magn} (%)	6.82	5.52	5.49	49.6	18.5
χ^2	2.048	1.905	1.905	2.169	2.002
μ_{Ru} (μ_B)	1.38(5)	1.49(5)	1.47(3)	1.41	1.50(11)

From Fig. 16(c) it can be seen that Γ_8 can readily be excluded. While the calculated Bragg intensities of the (111) and (002) reflections are more or less consistent with the data, no magnetic intensity is observed for the (002) reflection, which is calculated to be strong for Γ_8 order. While Γ_3 and Γ_{10} fit the data slightly better, Figs. 16(a) and 16(d) show they only allow for magnetic intensity on the (220) and (111) reflection, respectively (in the displayed 2θ range). As both reflections are observed, these IRs can be excluded. Γ_6 has two associated BVs [with moments either off-diagonal (along [211]) or coplanar (along [011])], fitting each individually gives an identical fit to the data describing all the observed magnetic Bragg scattering [Fig. 16(b) shows the fit of ψ_2 to the data]. Due to powder averaging we are unable to distinguish between these two BVs and/or determine whether the actual magnetic structure is a linear combination of the two. For this a single-crystal diffraction experiment will be required.

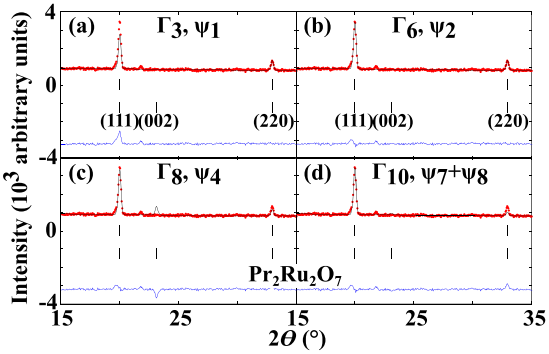

FIG. 16. Rietveld fits (solid black lines) of Γ_3 (a), Γ_6 (b), Γ_8 (c), and Γ_{10} (d), with ordered moments only on the Ru sublattice, to the neutron powder diffraction profile measured at $T = 1.5$ K for $Pr_2Ru_2O_7$ (•). The residual of the fits (blue lines) is shown at the bottom of the plots. The upper and lower tick marks indicate Bragg reflections coming from the crystal and magnetic structure of $Pr_2Ru_2O_7$, respectively.

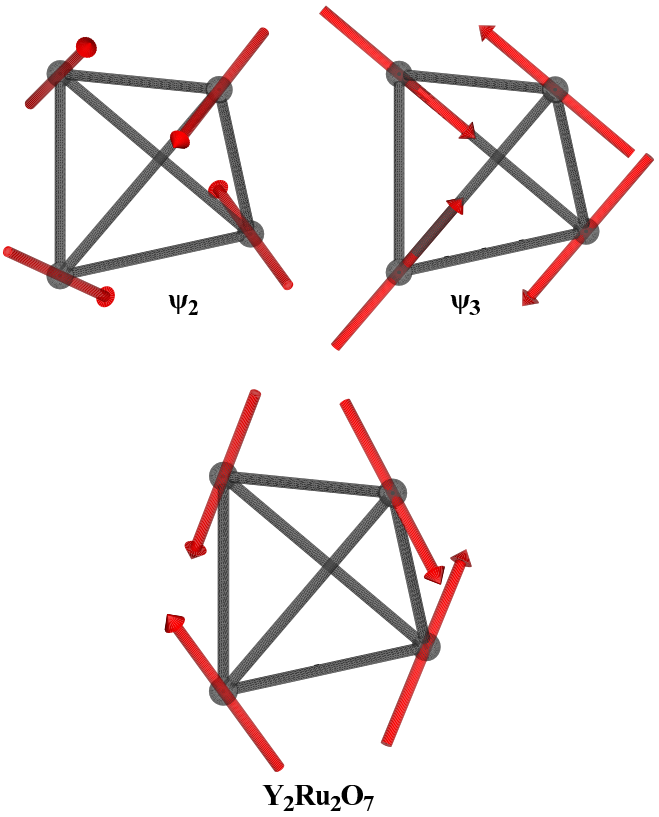

FIG. 17. Alignment of the magnetic Ru moments, according to ψ_2, ψ_3, and $Y_2Ru_2O_7$, within a single tetrahedra [31,74].

In summary, our analysis has shown that describing the ordering of the Ru moments in $x = 0$ either by the model proposed for $Y_2Ru_2O_7$ or by the IR Γ_6 of space group $Fd\bar{3}m$ gives identical fits to the data (Figs. 15 and 16). Closer examination of both models reveals that the two associated BVs of Γ_6 are special cases of the more general description used for $Y_2Ru_2O_7$ and these models are therefore identical (Fig. 17) [31]. Unlike what is found for the other magnetic rare-earth-containing Ru pyrochlores the IR associated with the Ru moments in $Pr_2Ru_2O_7$ is apparently unaffected by the Pr single-ion anisotropy [33,34]. The ordering inferred from powder diffraction for $Y_2Ru_2O_7$ and $Pr_2Ru_2O_7$ is presently indistinguishable from that inferred for $Er_2Ti_2O_7$, wherein the phase transition was recently ascribed to the order-by-disorder mechanism [75,76].

2. Temperature dependence

Figure 18 shows the temperature dependence of the ordered Ru moment, which was obtained by fitting the neutron power diffraction data using ψ_2 to describe the Ru ordering. The data clearly show the onset of an ordered Ru moment below 170 K, confirming that the anomaly observed in both the specific-heat and magnetization measurements at 165 K is associated with magnetic ordering of the Ru sublattice [15,77]. Upon cooling the size of the ordered moment increases, leveling off below 100 K to a value of $1.5\mu_B$. This is in line with what is observed in the other Ru pyrochlores [31,33,34].

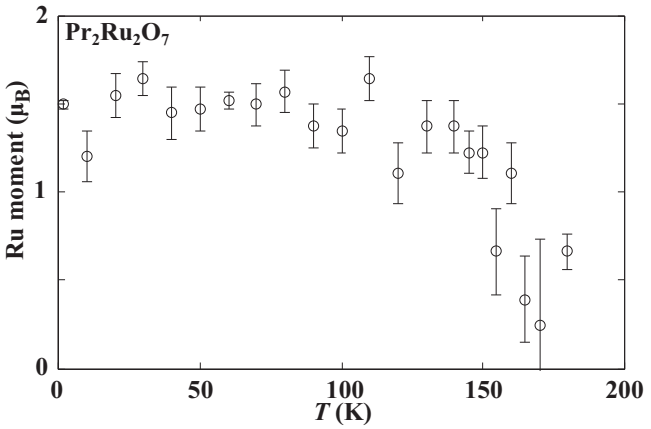

FIG. 18. Temperature dependence of the ordered Ru moment derived through Rietveld analysis of neutron diffraction data.

D. Low-energy magnetic response

Comparing the low-energy magnetic response of pure $Pr_2Ru_2O_7$ ($x = 0$) with that of the Bi-doped material ($x = 0.97$) in Fig. 9, we observe the following. In both samples, the wave-vector dependence of the inelastic magnetic scattering indicates it is associated with Pr^{3+} single-ion physics or is dominated by very short-range two-point spin correlations. The single-ion character of the inelastic scattering and the broadening of the spectral maximum with Bi doping indicates disorder plays a significant role. In $Pr_{2-x}Bi_xRu_2O_7$ for $x = 0.97$ (nonmagnetic and close to the insulator-to-metal transition), the presence of lone electron pairs on Bi may produce a low density of extended defects or a density wave which generates a continuum of local Pr environments that is temperature independent.

The EXAFS results show that environment about Bi is highly disordered for both $x = 0.97$ and 2. This disorder on those A-sites occupied by Bi will modify the CF experienced by neighboring Pr ions. Since Pr is a non-Kramers ion (and the doublet ground-state degeneracy relies on D_{3d} point-group symmetry) distortions of the local coordination environment can lift the doublet degeneracy. While this particular source of symmetry breaking is not present for $Pr_2Ru_2O_7$, the EXAFS data indicate significant distribution of Pr-O2 distances which may also split the doublet. Magnetoelastic effects due to the Ru-sublattice ordering are another possible origin of symmetry breaking on Pr sites. It has already been observed for $Y_2Ru_2O_7$ that magnetoelastic effects play an important role in the Ru magnetic ordering [78,79]. While no optical data are available for $Pr_2Ru_2O_7$, the ordering appears identical to that of $Y_2Ru_2O_7$, so the observed spin-phonon interactions that allow for ordering in $Y_2Ru_2O_7$ may also be present for $Pr_2Ru_2O_7$.

V. CONCLUSIONS

In our previous study of $Pr_{2-x}Bi_xRu_2O_7$, we showed the enhancement of the low-T specific-heat results from inhomogeneous splitting of the non-Kramers Pr doublet ground state and not heavy-fermion-type physics [37]. This inhomogeneous splitting was thought to arise from the disorder associated with substitution of Bi for Pr. To understand the magnetic

properties of these materials we performed EXAFS, elastic and inelastic neutron scattering measurements for $x = 0, 0.97$, and 2. The EXAFS measurements show the Ru environment (B-site) is well ordered throughout the series. On the A-site, the Pr environment has significant intrinsic disorder along the Pr-O2 axis which may contribute to splitting the non-Kramers doublet. The environment around Bi is highly disordered, which we attribute to an off-center displacement driven by the $6s$ lone pairs on Bi^{3+}.

In agreement with previously reported diffraction studies, Bi appears to displace in a direction midway between two O1 atoms. Our analysis of the CF measurements on both $x = 0$ and 0.97 show that the Pr ions, not taking into account the effect of local disorder as observed by EXAFS, have a doublet ground state and singlet first excited state in the pyrochlore structure. The high-energy inelastic neutron scattering data indicate strong CF phonon coupling is present in both systems.

The magnetic ordering of the Ru sublattice in $Pr_2Ru_2O_7$ is similar to that of $Y_2Ru_2O_7$, which in turn is consistent with the magnetic structure transforming according to IR Γ_6 of space group $Fd\bar{3}m$ [31]. Ordering of the Ru moment thus is unaffected by the rare-earth ion anisotropy. Our high-resolution diffraction measurements detected no structural distortion associated with Ru ordering below T_N. A weak magnetoelastic effect that lowers the point-group symmetry of the rare-earth site when Ru orders and lifts the non-Kramers ground-state degeneracy of praseodymium, however, remains a possible explanation for the lack of an ordered Pr moment.

The low-energy magnetic response of $Pr_{2-x}Bi_xRu_2O_7$ features a Q-independent excitation associated with splitting of the Pr quasidoublet ground state. For $x = 0$ the spectrum is temperature dependent, while for $x = 0.97$ where the gap is larger, the spectrum is broad and temperature independent. The nature of the splitting of the (non-Kramers) doublet ground state thus changes with doping, going from intrinsic and/or magnetoelastically induced for $x = 0$ to Bi induced A-site disorder driven for $x = 0.97$. These measurements show the Pr ground state to be very sensitive to local perturbations. This is a critical factor when studying materials containing non-Kramers rare-earth ions including $Tb_2Ti_2O_7$, $Ho_2Ti_2O_7$, and $LiHo_xY_{1-x}F_4$ [80–82].

For $Pr_2Ru_2O_7$, we conclude that weak magnetoelastic strain associated with Ru spin order, undetected by high-resolution diffraction, and/or local structural disorder, that we do detect by EXAFS, acts as transverse fields that lift the non-Kramers ground-state degeneracy of Pr^{3+} and produce a quadrupolar singlet ground state. The temperature dependence of the low-energy spectrum, however, admits the possibility of nontrivial collective physics, the exploration of which is important and will require single-crystalline samples. The similarity of the crystal-field level scheme for $Pr_2Sn_2O_7$, $Pr_2Zr_2O_7$, and $Pr_2Hf_2O_7$ to that of $Pr_2Ru_2O_7$ further suggests that proximity to a quadrupolar singlet ground state may be important in those compounds too [58,69–72,83].

ACKNOWLEDGMENTS

The work at JHU and ISIS was supported by the US Department of Energy, office of Basic Energy Sciences, Division of Material Sciences and Engineering, under Grant No. DE-FG02-02ER45983 through 2008 and beyond that on Grant No. DE-FG02-08ER46544. The work at Rutgers was supported by NSF through Grant No. DMR-0103858 and by the DOE under Grant No. DE-FG02-07ER46382. Work done at the UCLM was supported by the Ramón y Cajal program through Grant No. RYC-2005-001064 and the Consejería de Educación y Ciencia of the Junta de Comunidades de Castilla-La Mancha through Grant No. PII1I09-0083-2105. Work performed at SNU was supported by the National Creative Research Initiative (Grant No. 2010-0018300). K.H.K. was partially supported by KOSEF through CSCMR. The EXAFS experiments were performed at the Stanford Synchrotron Radiation Lightsource (SSRL), which is supported by the US Department of Energy, Office of Science, Office of Basic Energy Sciences under Contract No. DE-AC02-76SF00515.

[1] J. E. Greedan, J. Mater. Chem. **11**, 37 (2001).
[2] P. W. Anderson, Phys. Rev. **102**, 1008 (1956).
[3] J. S. Gardner, M. P. Gingras, and J. E. Greedan, Rev. Mod. Phys. **82**, 53 (2010).
[4] C. Lacroix, P. Mendels, and F. Mila, *Introduction to Frustrated Magnetism* (Springer, Berlin, 2011).
[5] H. T. Diep, *Frustrated Spin Systems* (World Scientific, Singapore, 2013).
[6] L. Balents, Nature (London) **464**, 199 (2010).
[7] B. Normand, Contemp. Phys. **50**, 533 (2009).
[8] M. A. Subramanian and A. W. Sleight, in *Handbook on the Physics and Chemistry of Rare Earths*, edited by K. A. Gschneidner and L. Eyring (Elsevier, Amsterdam, 1993), Vol. 16, p. 225.
[9] H. Fukazawa and Y. Maeno, Phys. Rev. B **67**, 054410 (2003).
[10] O. Sakai, Y. Jana, R. Higashinaka, H. Fukazawa, S. Nakatsuji, and Y. Maeno, J. Phys. Soc. Jpn. **73**, 2829 (2004).
[11] P. Blaha, D. J. Singh, and K. Schwarz, Phys. Rev. Lett. **93**, 216403 (2004).
[12] J. E. Greedan, M. Sato, X. Yan, and F. S. Razavi, Solid State Commun. **59**, 895 (1986).
[13] I. Kézsmárki, N. Hanasaki, K. Watanabe, S. Iguchi, Y. Taguchi, S. Miyasaka, and Y. Tokura, Phys. Rev. B **73**, 125122 (2006).
[14] K. S. Lee, D. K. Seo, and M. H. Whangbo, J. Solid State Chem. **131**, 405 (1997).
[15] N. Tiara, M. Wakeshima, and Y. Hinatsu, J. Phys.: Condens. Matter **11**, 6983 (1999).
[16] N. Tiara, M. Wakeshima, and Y. Hinatsu, J. Mater. Chem. **12**, 1475 (2002).
[17] D. Yanagishima and Y. Maeno, J. Phys. Soc. Jpn. **70**, 2880 (2001).
[18] S. Nakatsuji, Y. Machida, Y. Maeno, T. Tayama, T. Sakakibara, J. van Duijn, L. Balicas, J. N. Millican, R. T. Macaluso, and J. Y. Chan, Phys. Rev. Lett. **96**, 087204 (2006).
[19] Y. Machida, S. Nakatsuji, Y. Maeno, T. Tayama, T. Sakakibara, and S. Onoda, Phys. Rev. Lett. **98**, 057203 (2007).
[20] Y. Taguchi, Y. Oohara, H. Yoshizawa, N. Nagaosa, and Y. Tokura, Science **291**, 2573 (2001).

[21] M. J. P. Gingras, C. V. Stager, N. P. Raju, B. D. Gaulin, and J. E. Greedan, Phys. Rev. Lett. **78**, 947 (1997).

[22] V. Dupuis, E. Vincent, J. Hammann, J. E. Greedan, and A. S. Wills, J. Appl. Phys. **91**, 8384 (2002).

[23] H. J. Silverstein, K. Fritsch, F. Flicker, A. M. Hallas, J. S. Gardner, Y. Qiu, G. Ehlers, A. T. Savici, Z. Yamani, K. A. Ross *et al.*, Phys. Rev. B **89**, 054433 (2014).

[24] H. Sakai, K. Yoshimura, H. Ohno, H. Kato, S. Kambe, R. E Walstedt, T. D. Matsuda, Y. Haga, and Y. Onuki, J. Phys.: Condens. Matter **13**, L785 (2001).

[25] M. Hanawa, Y. Muraoka, T. Tayama, T. Sakakibara, J. Yamaura, and Z. Hiroi, Phys. Rev. Lett. **87**, 187001 (2001).

[26] S. Yonezawa, Y. Muraoka, Y. Matsushita, and Z. Hiroi, J. Phys.: Condens. Matter **16**, L9 (2004).

[27] S. Yonezawa, Y. Muraoka, Y. Matsushita, and Z. Hiroi, J. Phys. Soc. Jpn. **73**, 819 (2004).

[28] S. Yonezawa, Y. Muraoka, and Z. Hiroi, J. Phys. Soc. Jpn. **73**, 1655 (2004).

[29] T. Takeda, M. Nagata, H. Kobayashi, R. Kanno, Y. Kawamoto, M. Takano, T. Kamiyama, F. Izumi, and A. W. Sleight, J. Solid State Chem. **140**, 182 (1998).

[30] M. Tachibana, Y. Kohama, T. Shimoyama, A. Harada, T. Taniyama, M. Itoh, H. Kawaji, and T. Atake, Phys. Rev. B **73**, 193107 (2006).

[31] M. Ito, Y. Yasui, M. Kanada, H. Harashina, S. Yoshii, K. Murata, M. Sato, H. Okumura, and K. Kakurai, J. Phys. Soc. Jpn. **69**, 888 (2000); J. Phys. Chem. Solids **62**, 337 (2001).

[32] M. Rams, A. Zarzycki, A. Pikul, and K. Tomala, J. Magn. Magn. Mater. **323**, 1490 (2011).

[33] C. N. R. Wiebe, J. S. Gardner, S.-J. Kim, G. M. Luke, A. S. Wills, B. D. Gaulin, J. E. Greedan, I. Swainson, Y. Qiu, and C. Y. Jones, Phys. Rev. Lett. **93**, 076403 (2004).

[34] N. Taira, M. Wakeshima, Y. Hinatsu, A Tobo, and K. Ohoyama, J. Solid State Chem. **176**, 165 (2003).

[35] M. K. Haas, R. J. Cava, M. Avdeev, and J. D. Jorgensen, Phys. Rev. B **66**, 094429 (2002).

[36] S. Lee, J. G. Park, D. T. Adroja, D. Khomskii, S. Streltsov, K. A. McEwen, H. Sakai, K. Yoshimura, V. I. Anisimov, D. Mori *et al.*, Nat. Mater. **5**, 471 (2006).

[37] J. van Duijn, K. H. Kim, N. Hur, D. Adroja, M. A. Adams, Q. Z. Huang, M. Jaime, S.-W. Cheong, C. Broholm, and T. G. Perring, Phys. Rev. Lett. **94**, 177201 (2005).

[38] M. Avdeev, M. K. Haas, J. D. Jorgensen, and R. J. Cava, J. Solid State Chem. **169**, 24 (2002).

[39] A. L. Hector and S. B. Wiggin, J. Solid State Chem. **177**, 139 (2004).

[40] T. A. Vanderah, I. Levin, and M. W. Lufaso, Eur. J. Inorg. Chem. **2005**, 2895 (2005).

[41] S. J. Henderson, O. Shebanova, A. L. Hector, P. F. McMillan, and M. T. Weller, Chem. Mater. **19**, 1712 (2007).

[42] D. P. Shoemaker, R. Seshadri, A. L. Hector, A. Llobet, T. Proffen, and C. J. Fennie, Phys. Rev. B **81**, 144113 (2010).

[43] D. P. Shoemaker, R. Seshadri, M. Tachibana, and A. L. Hector, Phys. Rev. B **84**, 064117 (2011).

[44] Y. Machidaa, S. Nakatsuji, H. Tonomura, T. Tayama, T. Sakakibara, J. van Duijn, C. Broholm, and Y. Maeno, J. Phys. Chem. Solids **66**, 1435 (2005).

[45] D. L. Martin, Phys. Rev. B **8**, 5357 (1973).

[46] See http://lise.lbl.gov/RSPAK.

[47] J. Rodriguez-Carvajal, Phys. B (Amsterdam) **192**, 55 (1993).

[48] C. J. Carlile and M. A. Adams, Phys. B (Amsterdam) **182**, 431 (1992).

[49] V. G. Sakai, M. A. Adams, W. S. Howells, M. T. F. Telling, F. Demmel, and F. Fernandez-Alonso, RAL Technical Report No. RAL-TR-2011-004, 2011 (unpublished).

[50] P. Fabi, ISIS Technical Report No. RAL-TR-95-023, 1995 (unpublished).

[51] S. W. Lovesey, *Theory of Neutron Scattering from Condensed Matter* (Clarendon Press, Oxford, 1984).

[52] P. J. Brown, in *International Tabled for Crystallography*, edited by A. J. C. Wilson (Kluwer Academic, London, 1995), Vol. C.

[53] J. Jensen, J. Magn. Magn. Mater. **29**, 47 (1982).

[54] M. J. Hutchings, Solid State Phys. **16**, 227 (1964).

[55] S.-H. Lee, C. Broholm, M. F. Collins, L. Heller, A. P. Ramirez, Ch. Kloc, E. Bucher, R. W. Erwin, and N. Lacevic, Phys. Rev. B **56**, 8091 (1997).

[56] B. K. Teo, *EXAFS: Basic Principles and Data Analysis* (Springer, New York, 1986).

[57] A. L. Ankudinov, B. Ravel, J. J. Rehr, and S. D. Conradson, Phys. Rev. B **58**, 7565 (1998).

[58] K. Kimura, S. Nakatsuji, J.-J. Wen, C. Broholm, M. B. Stone, E. Nishibori, and H. Sawa, Nat. Commun. **4**, 1934 (2013).

[59] P. C. Hohenberg and W. F. Brinkman, Phys. Rev. B **10**, 128 (1974).

[60] G. Xu, C. Broholm, Y.-A. Soh, G. Aeppli, J. F. DiTusa, Y. Chen, M. Kenzelmann, C. D. Frost, T. Ito, K. Oka, and H. Takagi, Science **317**, 1049 (2007).

[61] L. Downward, C. H. Booth, W. W. Lukens, and F. Bridges, AIP Conf. Proc. **882**, 129 (2007).

[62] P. A. Lee and G. Beni, Phys. Rev. B **15**, 2862 (1977).

[63] A. Bianconi, in *X-ray Absorption: Principles, Applications, Techniques of EXAFS, SEXAFS and XANES*, edited by D. C. Koningsberger and R. Prins (Wiley, New York, 1988), p. 594.

[64] M. Loewenhaupt, M. Prager, E. Gratza, and B. Frick, J. Magn. Magn. Mater. **76-77**, 415 (1988).

[65] R. Schedler, U. Witte, M. Loewenhaupt, and J. Kudla, Phys. B (Amsterdam) **335**, 41 (2003).

[66] J. C. Nipko, M. Grimsditch, C.-K. Loong, S. Kern, M. M. Abraham, and L. A. Boatner, Phys. Rev. B **53**, 2286 (1996).

[67] C.-K. Loong, M. Loewenhaupt, J. C. Nipko, M. Braden, and L. A. Boatner, Phys. Rev. B **60**, R12549 (1999).

[68] D. T. Adroja, A. del Moral, C. de la Fuente, A. Fraile, E. A. Goremychkin, J. W. Taylor, A. D. Hillier, and F. Fernandez-Alonso, Phys. Rev. Lett. **108**, 216402 (2012).

[69] A. J. Princep, D. Prabhakaran, A. T. Boothroyd, and D. T. Adroja, Phys. Rev. B **88**, 104421 (2013).

[70] P. Bonville, S. Guitteny, A. Gukasov, I. Mirebeau, S. Petit, C. Decorse, M. C. Hatnean, and G. Balakrishnan, Phys. Rev. B **94**, 134428 (2016).

[71] R. Sibille, E. Lhotel, M. C. Hatnean, G. Balakrishnan, B. Fåk, N. Gauthier, T. Fennell, and M. Kenzelmann, Phys. Rev. B **94**, 024436 (2016).

[72] V. K. Anand, L. Opherden, J. Xu, D. T. Adroja, A. T. M. N. Islam, T. Herrmannsdörfer, J. Hornung, R. Schönemann, M. Uhlarz, H. C. Walker *et al.*, Phys. Rev. B **94**, 144415 (2016).

[73] A. S. Wills, Phys. B (Amsterdam) **276**, 680 (2000).

[74] K. Momma and F. Izumi, J. Appl. Crystallogr. **44**, 1272 (2011).

[75] A. Poole, A. S. Wills, and E. Lelièvre-Berna, J. Phys.: Condens. Matter **19**, 452201 (2007).

[76] L. Savary, K. A. Ross, B. D. Gaulin, J. P. C. Ruff, and L. Balents, Phys. Rev. Lett. **109**, 167201 (2012).
[77] N. Taira, M. Wakeshima, and Y. Hinatsu, J. Solid State Chem. **152**, 441 (2000).
[78] J. S. Lee, T. W. Noh, J. S. Bae, In-Sang Yang, T. Takeda, and R. Kanno, Phys. Rev. B **69**, 214428 (2004).
[79] J. van Duijn, N. Hur, J. W. Taylor, Y. Qiu, Q. Z. Huang, S.-W. Cheong, C. Broholm, and T. G. Perring, Phys. Rev. B **77**, 020405 (2008).
[80] J. S. Gardner, S. R. Dunsiger, B. D. Gaulin, M. J. P. Gingras, J. E. Greedan, R. F. Kiefl, M. D. Lumsden, W. A. MacFarlane, N. P. Raju, J. E. Sonier *et al.*, Phys. Rev. Lett. **82**, 1012 (1999).
[81] M. J. Harris, S. T. Bramwell, D. F. McMorrow, T. Zeiske, and K. W. Godfrey, Phys. Rev. Lett. **79**, 2554 (1997).
[82] J. Brooke, D. Bitko, T. F. Rosenbaum, and G. Aeppli, Science **284**, 779 (1999).
[83] S. Petit, E. Lhotel, S. Guitteny, O. Florea, J. Robert, P. Bonville, I. Mirebeau, J. Ollivier, H. Mutka, E. Ressouche *et al.*, Phys. Rev. B **94**, 165153 (2016).